JOURNAL OF SPACECRAFT AND ROCKETS
Vol. 41, No. 2, March–April 2004

# X-38 Experimental Aerothermodynamics

Thomas J. Horvath,* Scott A. Berry,* and N. Ronald Merski†
*NASA Langley Research Center, Hampton, Virginia 23681*
and
Steve M. Fitzgerald‡
*NASA Johnson Space Center, Houston, Texas 77058*

**An overview is provided of the hypersonic aerothermodynamic wind-tunnel program conducted at the NASA Langley Research Center in support of the X-38 development. Global and discrete surface heat transfer, force and moment, surface streamline patterns, and shock shapes were measured on scaled models of the proposed X-38 configuration in different test gases at Mach 6, 10, and 20. The test parametrics include angles of attack from 0 to 50 deg; unit Reynolds numbers from $0.3 \times 10^6$ to $16 \times 10^6$/ft: rudder deflections of 0, 2, and 5 deg; and body-flap deflections from 0 to 30 deg in 2.5-deg increments. Results from hypersonic aerodynamic screening studies that were conducted as the configuration evolved to the present shape are presented. Heavy gas simulation tests have indicated that the primary real-gas effects on X-38 aerodynamics at trim conditions are expected to favorably influence flap effectiveness. Comparisons of the experimental heating and force and moment data to prediction and the current aerodynamic data book are highlighted. The effects of discrete roughness elements on boundary-layer transition were investigated at Mach 6, and the development of a transition correlation for the X-38 vehicle is described. Extrapolation of ground-based heating measurements to flight radiation equilibrium wall temperatures at Mach 6 and 10 were made and generally compared to within 50°F of flight prediction.**

## Nomenclature

$b_{\text{ref}}$ = reference span, in.
$C_A$ = axial-force coefficient, $A/qS_{\text{ref}}$
$C_m$ = pitching-moment coefficient, $m/qL_{\text{ref}}S_{\text{ref}}$
$C_N$ = normal-force coefficient, $N/qS_{\text{ref}}$
$C_{l\beta}$ = rolling-moment derivative, 1/deg
$C_{n\beta}$ = yawing-moment derivative, 1/deg
$C_{Y\beta}$ = side-force derivative, 1/deg
$H$ = enthalpy, BTU/lbm
$h$ = heat-transfer coefficient, lbm/ft$^2$-s; $\dot{q}/(H_{\text{aw}} - H_w)$, where $H_{\text{aw}} = H_{t,2}$
$h_{\text{ref}}$ = reference heat-transfer coefficient using Fay–Riddell calculation to stagnation point of scaled X-38
$k$ = boundary-layer trip height, in.
$L/D$ = lift-to-drag ratio
$L_{\text{ref}}$ = reference length, in.
$M$ = Mach number
$P$ = pressure, psia
$q$ = dynamic pressure, psi
$\dot{q}$ = heat-transfer rate, BTU/ft$^2$-s
$R$ = radius, in.
$Re$ = unit Reynolds number, 1/ft
$S_{\text{ref}}$ = reference area, in.$^2$
$T$ = temperature, °F
$t$ = time, s
$x$ = axial distance from origin, in.
$y$ = lateral distance from origin, in.
$\alpha$ = angle of attack, deg
$\beta$ = sideslip angle, deg
$\gamma$ = ratio of specific heats
$\delta$ = boundary-layer height, in.
$\delta_{\text{BF}}$ = control-surface deflection, deg
$\rho$ = density, lbm/in.$^3$

*Subscripts*

aw = adiabatic wall
$n$ = model nose
$t$, 1 = reservoir conditions
$w$ = wall
$\theta$ = boundary-layer momentum thickness, in.
2 = stagnation conditions behind normal shock
$\infty$ = freestream conditions

Received 14 July 2000; revision received 19 December 2002; accepted for publication 17 January 2003. 

*Aerospace Technologist, Aerothermodynamics Branch.
†Aerospace Technologist, Aerothermodynamics Branch. Member AIAA.
‡Deputy Chief, GN&C Design and Analysis Branch.

## Introduction

THE NASA X-38 program sought to demonstrate an autonomously returned orbital test flight vehicle to support the development of an operational crew return vehicle[1] (CRV) for the International Space Station (ISS). A test flight of a prototype vehicle returning from low Earth orbit was intended to demonstrate the entire mission profile of returning space station crew members safely back to Earth in the event of medical or mechanical problems and shuttle unavailability. The X-38 full-scale technology demonstrator vehicle[2] built by NASA Johnson Space Center (JSC) sought to validate key design and operational aspects for the CRV. Integral to the formulation of the X-38 flight data book and the design of the thermal protection system, the aerothermodynamic environment was defined through a synergistic combination of ground-based testing and computational fluid dynamics. Conceived to demonstrate CRV technologies, the X-38 design was considered flexible enough to evolve to a crew transfer vehicle (CTV). The potential for CRV/CTV dual use led to a cooperative NASA/European effort of the X-38 design.[3,4] A CTV design would have permitted vehicle integration to an expendable booster, such as the French Ariane 5, permitting personnel to be ferried to and from the station. Budget constraints associated with the space station in 2002 forced the agency to terminate the CRV program and the X-38 technology demonstrator vehicle.

The X-38 CRV technology demonstrator mission originally planned for 2005 called for a 28.5-ft-long vehicle (designated as V201) to be released from a shuttle positioned in a high-inclination ISS orbit. Following the jettison of a deorbit engine module, the X-38 would have returned unpowered (similar to the space shuttle)

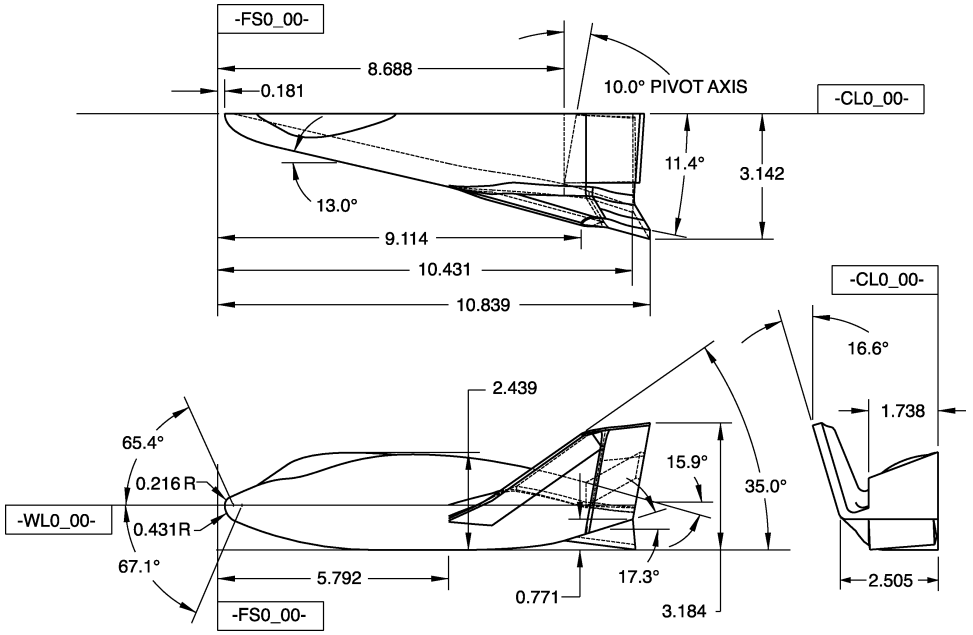


**Fig. 1 Dimensions (in inches) for 0.0295-scale X-38 Rev-3.1.**

and then used a steerable parafoil,[5] a technology first developed by the U.S. Army, for its final descent. Landing would be accomplished on skids rather than wheels.

Consistent with the X-38 program's goal to take advantage of available equipment and technology to reduce vehicle development costs by an order of magnitude.[6,7] the shape of the X-38 drew upon a synthesis of work performed by the U.S. government and industry over the past few decades.[8,9] The initial X-38 shape (shown in Fig. 1 at 0.0295 scale) proposed by NASA JSC was based on a lifting-body concept originally developed and flown during the U.S. Air Force PRIME (X-23/SV-5D)[10,11] and PILOT (X-24A)[12] projects in the mid-1960s and early 1970s. Referred to as Rev 3.1, this lifting-body configuration was initially selected by JSC for the CRV mission because of its relatively high hypersonic $L/D$; higher $L/D$ translates to larger cross-range capability, shorter loiter times in orbit, and volumetric efficiency (room for all station crew if necessary). The current shape (Rev 8.3) departs from the X-23/X-24A and the initial Rev 3.1 configurations in that it reflects changes to the vehicle upper surface to accommodate CTV missions should NASA and its international partners decide to pursue this option. High approach speeds and long rollout distances associated with the low subsonic $L/D$ from this lifting body require that the landing be augmented with a steerable parafoil.[13] This critical feature for injured or incapacitated crew permits the CRV to land within close proximity of medical facilities with minimal $g$ loads.

Under the NASA/European partnership Daussault Aviation served as prime contractor for the development of X-38 aerodynamic and aerothermodynamic databases.[14,15] The role of the NASA Langley Research Center (LaRC) Aerothermodynamics Branch (AB) has been to provide hypersonic laminar and turbulent global surface heating and force and moment (F&M) data for computational-fluid-dynamics (CFD) validation and to serve as a cross check of X-38 data obtained in European facilities. Results from early LaRC wind-tunnel heating tests on the initial Rev 3.1 compared favorably to CFD computations.[16,17] Transition data were obtained,[18] which when compared to similar measurements made on the shuttle[19] supported the use of a $Re_\theta/M_e$ criterion[15] for assessment of manufacturing (step) tolerances of the thermal-protection-system (TPS) tiles. Hypersonic aerodynamic screening studies on Rev 3.1 were conducted at LaRC to assess the potential for real-gas effects.[20] Since the time of these publications, additional aerodynamic and aeroheating tests have been completed, which addressed design changes to the vehicle outer mold lines. In addition, the original experimental database has been supplemented to include the complex thermal design environments on the X-38 (e.g., region behind split-deflected body flaps). In this area LaRC wind-tunnel data in the form of discrete measurements have served as the primary source of heating information.

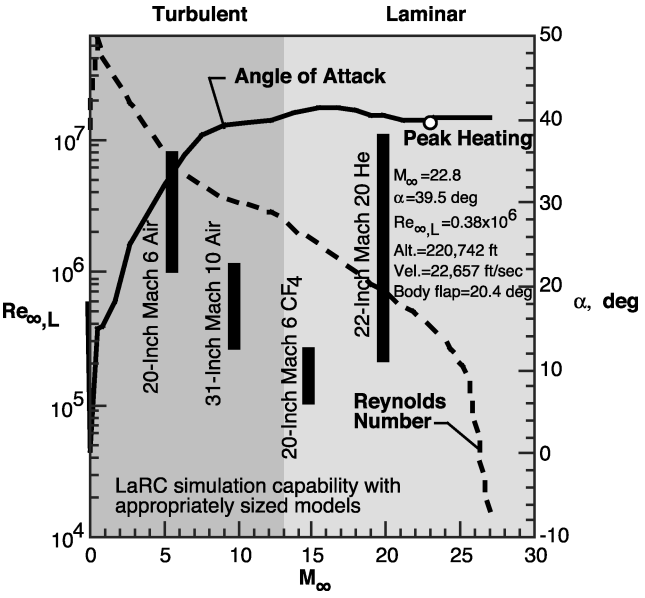


**Fig. 2 X-38 cycle 8 trajectory.**

The purpose of this paper is to present an overview of the LaRC AB experimental program to characterize the X-38 hypersonic aerothermodynamic environment. As discussed in Ref. 21, the term "aerothermodynamics" is taken to encompass aerodynamics, aeroheating, and fluid dynamics. The experimental results were obtained in the Langley Aerothermodynamic Laboratories (LAL).[22] Over 1500 tunnel runs from 16 different entries in four facilities have been completed since May 1996. Table 1 lists all of the LaRC wind-tunnel tests to date in support of X-38 aerothermodynamics. In terms of Mach- and Reynolds-number simulation, an X-38 flight trajectory considered by NASA JSC (designated as cycle 8) has indicated that the 28.5-ft-long flight vehicle would experience length Reynolds numbers $Re_L$ of approximately $0.7 \times 10^6$, $3.6 \times 10^6$, and $6 \times 10^6$ at freestream Mach numbers of 20, 10, and 6, respectively (Fig. 2). Figure 2 also indicates the corresponding range of length

**Table 1 X-38 tests in NASA LaRC Aerothermodynamics Branch tunnels**

| Year | Tunnel | Test | Runs | Configuration(s) | Objective |
|---|---|---|---|---|---|
| 1996 | 22-In. Mach 20 He | 556 | 35 | Rev 3.0/Rev 3.1 | F&M initial screening |
| 1996 | 31-In. Mach 10 Air | 322 | 42 | Rev 3.0 | Heating initial screening |
| 1996 | 22-In. Mach 20 He | 560 | 20 | YPAIO | F&M revised OML |
| 1996 | 20-In. Mach 6 CF4 | 113 | 56 | Rev 3.1/YPAIO | F&M gamma effects |
| 1996 | 20-In. Mach 6 Air | 6722 | 6 | Rev 3.1 | F&M schlieren |
| 1996 | 20-In. Mach 6 Air | 6733 | 90 | Rev 3.1/YPAIO | F&M gamma effects |
| 1996 | 20-In. Mach 6 Air | 6735 | 174 | Rev 3.1 | Heating transition |
| 1997 | 31-In. Mach 10 Air | 335 | 197 | Rev 3.1/YPAIO | F&M Mach effects |
| 1998 | 20-In. Mach 6 CF4 | 120 | 47 | Rev 8.3 | F&M screening new OML |
| 1998 | 20-In. Mach 6 Air | 6765 | 50 | Rev 8.3 | F&M screening new OML |
| 1998 | 31-In. Mach 10 Air | 345 | 122 | Rev 8.3 | F&M Mach effects |
| 1998 | 20-In. Mach 6 Air | 6774 | 138 | Rev 8.3 | F&M gamma effects |
| 1998 | 20-In. Mach 6 CF4 | 123 | 50 | Rev 8.3 | F&M gamma effects |
| 1998 | 20-In. Mach 6 CF4 | 125 | 143 | Rev 8.3 | F&M gamma effects |
| 1999 | 20-In. Mach 6 Air | 6782 | 216 | Rev 8.3 | Heating global/cavity |
| 2000 | 31-In. Mach 10 Air | 368 | 53 | Rev 8.3 | Heating global |

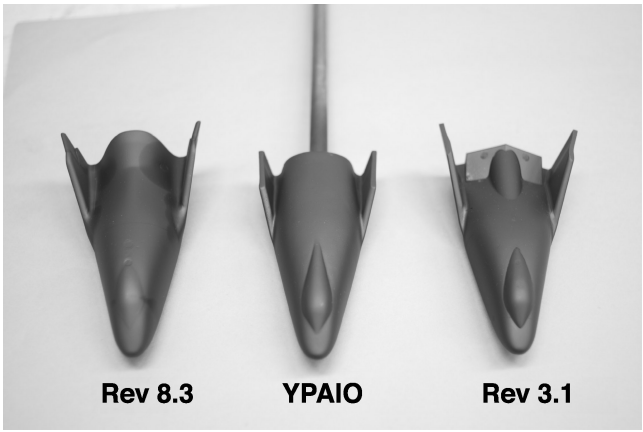


**Fig. 3 The 0.0175-scale metallic F&M models.**

Reynolds number that can be produced in the LAL with an appropriately sized model for each facility. Heating predictions along the cycle 8 flight trajectory would place peak heating to the stagnation point of a reference sphere near Mach 23 at $\alpha = 40$ deg.

Test techniques that were utilized include thermographic phosphors and thin-film thermometry, which provide global and discrete surface heating, respectively; oil flow, which provides surface streamline information; schlieren, which provides shock details; and a six-component strain-gauge balance to provide aerodynamic F&M loads. Parametrics from the tests conducted in four facilities were Mach numbers of 6,10, and 20; normal shock density ratios of 4 to 12 produced in three test gases; a range of angle of attack from 0 to 50 deg; unit Reynolds number of 0.3 to $16 \times 10^6$/ft; and body-flap deflections from 0 to 30 deg in 2.5-deg increments.

## Experimental Methods

### Models

The evolution of the X-38 outer mold lines (OML) to the present shape (Rev 8.3) is highlighted in Fig. 3 (a photograph of the various 0.0175 model scale force and moment models). All proposed vehicle configurations incorporated symmetric fins with deflectable rudders and two body flaps that deflect away from the lower (windward) fuselage for aerodynamic control. The progression of OML modifications shown (Rev 3.1, YPAIO, and Rev 8.3) are indicative of changes made to the upper fuselage (leeside). The windward surface has essentially retained the same basic shape as the SV-5D lifting bodies flown in the 1960s. Two basic model lengths (6 and 10 in.), determined by facility test core size, resulted in selected model scale factors of 1.75 and 2.95%.

As the LaRC test results were to provide benchmark data, model mold-line accuracy relative to the CFD surface grid definition was important. This type of quality control was also necessary because of the complementary tests conducted in Europe on separate models. To ensure precision, numerically controlled milling machines were utilized in the fabrication of the X-38 family of F&M wind-tunnel models utilizing CAD geometry supplied by JSC. Rapid prototyping/casting techniques[23,24] were used for construction of the heat-transfer models to provide an early assessment of the heating environment. The manufacturing tolerance for the machined metallic models was $\pm 0.003$ in. on dimensions with surfaces polished to a 32-$\mu$in. (rms) finish. The manufacturing tolerance for the cast ceramic or resin models was $\pm 0.007$ in. on dimensions. The distributed roughness associated with phosphor coatings sprayed on ceramic models has been measured and is typically within 350–500 $\mu$in. (rms).

*Forces and Moments*

Initial aerodynamic screening studies on X-38 conducted in the unheated 22-Inch Mach 20 Helium Tunnel utilized resin models for testing as temperature was not an issue. Two 6-in. (0.0175-scale) resin models were fitted internally with a steel sleeve in order to accept a balance. The models were designed to accept body flaps of various deflections.

Later studies on Rev 3.1 and Rev 8.3 conducted in the heated tunnels of the Langley Aerothemodynamic Laboratories required the use of metallic models. The bodies of these two 6-in. models (Rev 3.1 and Rev 8.3) were fabricated from aluminum, whereas the nose, fins, and control surfaces were 15-5 stainless steel. As with the earlier resin models, the metallic models incorporated multiple control-surface settings and internally fitted with interchangeable steel sleeves to accept several different balances.

*Heat Transfer*

Two types of heat-transfer models were fabricated: 1) a series of cast silica ceramic models for global heating information and 2) two thin-film models providing discrete measurements. At LaRC the global phosphor technique has largely replaced the thin-film technique caused by the dramatic reduction in model fabrication time and instrumentation costs. Although these benefits are revolutionary, the technique can have limitations where fast (sensor) response times are desired or the optical view of the model surface is limited. In the present X-38 heating studies the required optical view behind the deflected body flaps was limited. Thin-film instrumentation was used to compliment the global technique during this phase of testing.

*Global phosphor thermography.* More than 40 cast ceramic models were fabricated in support of the LaRC X-38 aerothermodynamic program, all of which share a common construction technique. A rapid prototyping technique was first used to build a resin stereolithography (SLA) model with various, detachable body flaps on both the port and starboard region of the base of

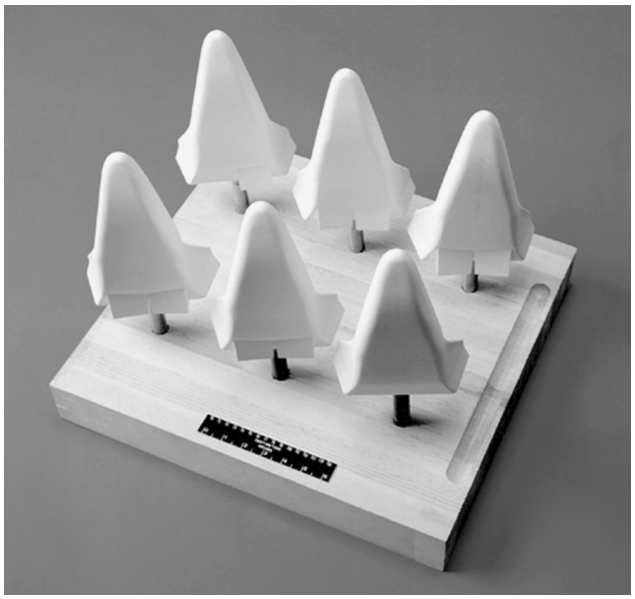

**Fig. 4 The 0.0295-scale ceramic heat-transfer models.**

the vehicle. The SLA resin model was then assembled with the desired control-surface settings and served as a pattern to construct molds from which the cast ceramic model configurations were made. A magnesia ceramic was used to backfill the ceramic shells, thus providing strength and support to the sting support structure.

A photograph of six ceramic 0.0295-scale (10-in.) Rev 3.1 model configurations with various body-flap deflections is shown in Fig. 4. Typically, two casts of each configuration were made, the primary being immediately prepared for testing and the backup shell held in reserve, in case of problems with the primary. To obtain accurate heat-transfer data with the phosphor technique, the models are cast with a material with low thermal diffusivity and well-defined, uniform, isotropic thermal properties. The phosphor coatings typically do not require refurbishment between runs in the wind tunnel and have been measured to be approximately 0.001 in. thick. Details concerning the model fabrication technique and phosphor coating can be found in Refs. 18 and 24. Fiducial marks were placed on the model surface to assist in determining spatial locations accurately. Once the phosphor testing was completed, the untested backup models were prepared (spray coated and kiln fired with a thin black glazing) for use as oil-flow and schlieren models.

*Discrete thin film.* Two metallic models were constructed and fitted with a machinable ceramic insert instrumented on the surface with small resistance thermometers. The first model, cast with aluminum, was created from a mold that used a resin SLA model as a pattern. This SLA resin model was identical to the pattern used to construct the cast ceramic phosphor heating models. The second model was unique in the sense that it was the first rapid prototype, selective laser-sintered metallic model successfully tested in a LaRC wind tunnel. In contrast to the more conventional rapid prototyping techniques that utilize resins or wax to create a pattern from which the actual tunnel model is cast, this technique omits the intermediate step by "building" the model, layer by layer, using a metallic powder. Originally, this model was intended as a backup to the cast aluminum model. Surface verification measurements indicated that the laser-sintered model was superior to the cast aluminum model in terms of linear shrinkage. Based on these results, it was decided to instrument and test this model as well.

A photograph of the 0.0295-scale (10-in.) Rev 8.3 thin-film model installed in the Mach 6 air tunnel is shown in Fig. 5. The cavity region behind the deflected body flaps was instrumented (Fig. 5a inset) with thin-film gauges to characterize the local heating in a region with restricted optical access. Sixty-eight sensors were placed at

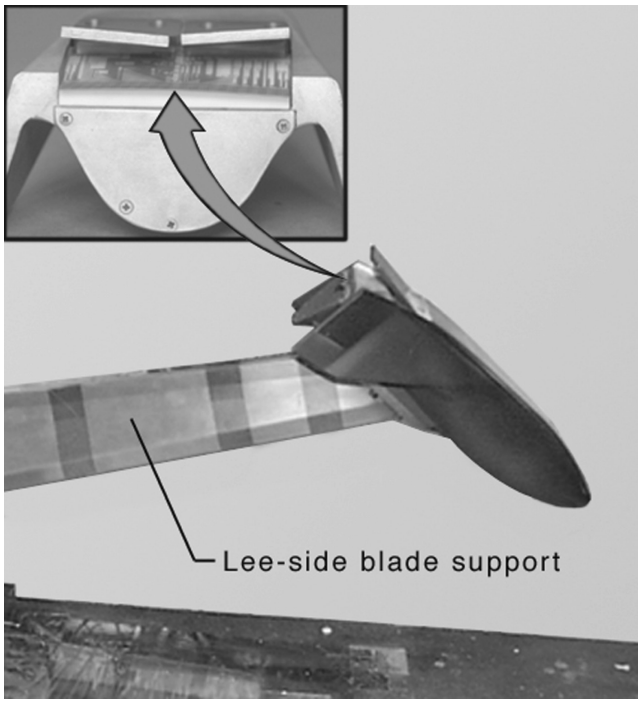


**Fig. 5a Thin-film heat-transfer model installed in the NASA LaRC 20-Inch Mach 6 Air Tunnel.**

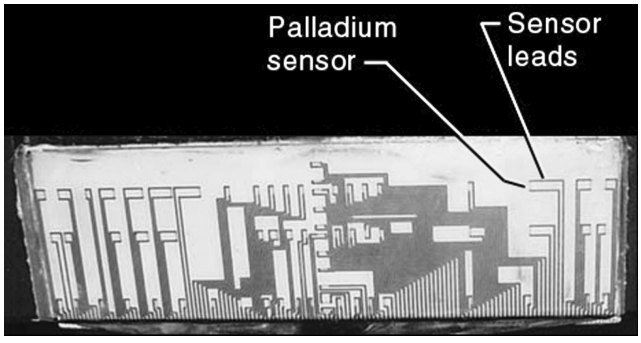


**Fig. 5b Flap cavity thin-film heat-transfer sensors.**

predetermined locations on the Macor (trademark of Corning Glass Works) substrate (Fig. 5b).

### Facility Descriptions

At the time of the X-38 experimental test program, the LAL consisted of five hypersonic wind tunnels that collectively provided a wide range of Mach number, unit Reynolds number, and normal shock density ratio.[22] This range of hypersonic simulation parameters is caused, in part, by the use of three different test gases (air, helium, and tetrafluoromethane), thereby making several of the facilities unique national assets. The LAL are relatively small and economical to operate, hence ideally suited for fast-paced aerodynamic performance and aeroheating studies aimed at screening, assessing, optimizing, and benchmarking (when combined with computational fluid dynamics) advanced aerospace vehicle concepts and basic fundamental flow physics research.

#### *20-Inch Mach 6 Air Tunnel*

Heated, dried, and filtered air is used as the test gas. Typical operating conditions for the tunnel are stagnation pressures ranging from 30 to 500 psia, stagnation temperatures from 760 to 1000°R, and freestream unit Reynolds numbers from 0.5 to $8 \times 10^6$/ft. A two-dimensional, contoured nozzle is used to provide nominal freestream Mach numbers from 5.8 to 6.1. The test section is $20.5 \times 20$ in; the nozzle throat is $0.399 \times 20.5$ in. A floor-mounted model injection system can insert models from a sheltered position

to the tunnel centerline in less than 0.5 s. Run times up to 15 min are possible with this facility for F&M and pressure measurements. For the heat-transfer and flow-visualization tests model residence time in the flow is only a few seconds.

*20-Inch Mach 6 CF4 Tunnel*

Heated, dried, and filtered tetrafluoromethane ($CF_4$) is used as the test gas. Typical operating conditions for the tunnel are stagnation pressures ranging from 85 to 2000 psia, stagnation temperatures up to 1300°R, and freestream unit Reynolds numbers from 0.01 to $0.3 \times 10^6$/ft. A contoured axisymmetric nozzle is used to provide nominal freestream Mach numbers from 5.9 to 6.01. The nozzle-exit diameter is 20 in. with the flow exhausting into an open-jet test section; the nozzle throat diameter is 0.466 in. A floor-mounted model injection system can inject models from a sheltered position to the tunnel centerline in less than 0.5 s. Nominal run time for F&M testing is approximately 20 s in this facility.

*31-Inch Mach 10 Air Tunnel*

Heated, dried, and filtered air is used as the test gas. Typical operating conditions for the tunnel are stagnation pressures ranging from 150 to 1350 psia, stagnation temperatures from 1750 to 1850°R, and freestream unit Reynolds numbers from 0.25 to $2 \times 10^6$/ft. A three-dimensional, contoured nozzle is used to provide nominal freestream Mach number of 10. The test section is $31 \times 31$ in.; the nozzle throat is $1.07 \times 1.07$ in. A side-mounted model injection system can insert models from a sheltered position to the tunnel centerline in less than 0.5 s. Run times up to 1.5 min are possible with this facility, although for heat-transfer and flow-visualization tests the model residence time required in the flow is only a few seconds.

*22-Inch Mach 20 Helium Tunnel*

Heated or unheated, dried, purified, and filtered helium is used as the test gas. Typical operating conditions for the tunnel are stagnation pressures ranging from 300 to 3300 psia, stagnation temperatures from 490 to 900°R, and freestream unit Reynolds numbers from 2.5 to $22 \times 10^6$/ft. A contoured axisymmetric nozzle is used to provide nominal freestream Mach numbers from 18.1 to 22.3. The nozzle exit diameter is 22 in. with the flow exhausting into an open-jet test section; the nozzle throat diameter is 0.622 in. A floor-mounted model injection system can insert models from a sheltered position to the tunnel centerline in less than 0.5 s. Run times up to 30 s are possible with this facility.

**Test Conditions and Setup**

Nominal reservoir and corresponding freestream flow conditions for the four tunnels are presented in Table 2. The freestream properties were determined from the measured reservoir pressure and temperature and the measured pitot pressure at the test section (or inferred from previous calibrations). Test-section wall static and pitot pressures were monitored where possible and compared to tunnel empty conditions to assess if model blockage effects existed. No significant differences in pitot pressure were measured, and it was concluded that significant blockage did not exist. The ratio of projected model frontal area ($\alpha = 40$ deg) to tunnel cross-sectional area for the 0.0175-scale model was less than 0.1.

All heating and force and moment models were supported by a base-mounted cylindrical sting with the exception of the two thin-film, heat-transfer models, which were blade supported from the upper surface. This installation was done to minimize possible support interference associated with the flap cavity measurements. Details of the X-38 ceramic heat-transfer model installation in the NASA LaRC 20-Inch Mach 6 Air Tunnel can be found in Ref. 18.

**Test Techniques**

*Forces and Moments*

Aerodynamic force and moment loads were measured throughout the test program using several sting-supported, six-component, water-cooled, internal strain-gauge balances. Balance temperature was monitored using integrated water jacket thermocouples to ensure excessive thermal gradients did not develop during the test run. Typically, the aerodynamic models were positioned in the test core flow on the tunnel centerline. In the $CF_4$ tunnel the model was located approximately 1.0 in. downstream of the nozzle exit and laterally displaced 4 in. from the tunnel centerline to avoid small disturbances that are characteristic in axisymmetric nozzles. Limited tests made with the model on tunnel centerline did not indicate any measurable effect on the aerodynamic characteristics of the present configuration for the range of angle of attack tested.

*Phosphor Thermography*

Advances in image-processing technology, which have occurred in recent years, have made digital optical measurement techniques practical for wind-tunnel applications. One such optical acquisition method is two-color relative-intensity phosphor thermography,[25–27] which has been utilized in several aeroheating tests conducted in the hypersonic wind tunnels of the NASA Langley Research Center.[19,28,29] With this technique ceramic wind-tunnel models are fabricated and coated with phosphors that fluoresce in two regions of the visible spectrum when illuminated with ultraviolet light. The fluorescence intensity is dependent on the amount of incident ultraviolet light and the local surface temperature of the phosphors. By acquiring fluorescence intensity images with a color video camera of an illuminated phosphor model exposed to flow in a wind tunnel, surface-temperature mappings can be calculated on the portions of the model that are in the field of view of the camera. A temperature calibration of the system conducted prior to the study provides tables used to convert the ratio of green and red intensity images to global temperature mappings. With temperature images acquired at different times during a wind-tunnel run, global heat-transfer images are computed assuming one-dimensional semi-infinite heat conduction. The primary advantage of the phosphor technique is the global resolution of the quantitative heat-transfer data. Such data can be used to identify the heating footprint of complex, three-dimensional flow phenomena (e.g., transition fronts, turbulent wedges, boundary-layer vortices, etc.) that are extremely difficult to resolve by discrete measurement techniques. Because models are fabricated and instrumented more rapidly and

**Table 2 Nominal flow conditions in NASA LaRC Aerothermodynamic Laboratories**

| Facility | $M_\infty$ | $q_\infty$, psi | $P_{t,1}$, psi | $T_{t,1}$, °F | $\rho_2/\rho_\infty$ | $Re_\infty$/ft ($\times 10^6$) |
|---|---|---|---|---|---|---|
| 22-In. Mach 20 He | 17.4 | 1.25 | 500 | 80 | 4.0 | 3.99 |
| 31-In. Mach 10 air | 9.7 | 0.66 | 350 | 1350 | 5.96 | 0.53 |
| | 9.83 | 1.25 | 720 | 1350 | 5.98 | 1.01 |
| | 9.95 | 2.41 | 1450 | 1350 | 5.98 | 2.00 |
| 20-In. Mach 6 air | 5.91 | 0.51 | 30 | 410 | 5.23 | 0.53 |
| | 5.90 | 1.04 | 60 | 430 | 5.23 | 1.04 |
| | 5.94 | 2.10 | 125 | 450 | 5.27 | 2.08 |
| | 5.98 | 4.07 | 250 | 450 | 5.28 | 4.06 |
| | 6.02 | 7.52 | 475 | 475 | 5.29 | 7.28 |
| 20-In. Mach 6 $CF_4$[a] | 5.98 | 0.80 | 950 | 850 | 11.68 | 0.35 |

[a]Mach 15–20 simulation caused by high normal shock density ratio $\rho_2/\rho_\infty$ and/or low values of specific heat ratio $\gamma$ within shock layer.

economically, global phosphor thermography has largely replaced discrete heating instrumentation in the LAL.

*Thin Film*

Thin-film resistance gauges were used to infer convective heating in the region behind the deflected body flaps where optical access was limited. Standard mechanical deposition techniques[30] developed at LaRC were used to fabricate the $0.030 \times 0.040$ in. platinum sensing elements. Measured surface temperatures were integrated over time to determine the local heat-transfer rate using the 1DHEAT code developed by Hollis.[31] Both analytical[32,33] and numerical finite volume heat-transfer models are incorporated into this code. The analytical solutions are derived from one-dimensional, semi-infinite solid heat-conduction theory with the assumption of constant substrate (model wall) thermal properties. When using the analytical option, the inferred heating rates are empirically corrected for the effects of variable model thermal properties. For the present study the uncertainty associated with variable wall thermal properties is believed to be minimal, particularly in the flap cavity region where surface temperature increases of 5°F or less were measured.

*Flow Visualization*

Flow visualization in the form of schlieren and oil-flow techniques was used to complement the surface heating and F&M tests. The LaRC 20-Inch Mach 6 air and $CF_4$ tunnels are equipped with a pulsed white-light, Z-pattern, single-pass schlieren system with a field of view encompassing the entire test core. Images were recorded on a high-resolution digital camera and enhanced with commercial software. The 31-Inch Mach 10 air and 22-Inch Mach 20 He tunnels do not have schlieren systems.

Surface streamline patterns were obtained using the oil-flow technique. Backup ceramic models or the metallic force models were spray painted black to enhance contrast with the white pigmented oils used to trace streamline movement. A thin basecoat of clear silicon oil was first applied to the surface, and then a mist of pinhead-sized pigmented-oil drops was applied onto the surface. After the model surface was prepared, the model was injected into the airstream, and the development of the surface streamlines was recorded with a conventional video camera. The model was retracted immediately following flow establishment and formation of streamline patterns, and postrun digital photographs were taken.

**Data Reduction and Uncertainty**

A 16-bit analog-to-digital facility data-acquisition system acquired flow condition data. Measured values of $P_{t,1}$ and $T_{t,1}$ are estimated to be accurate to within $\pm 2\%$.

Heating rates were calculated from the global surface temperature measurements using one-dimensional semi-infinite solid heat-conduction equations.[27] Acquisition of the surface-temperature data was made at the earliest possible time so as to preserve the semi-infinite solid assumption even for areas such as the body flap and fin. In regions of large temperature gradients or small radius of curvature (such as the nosecap and fin leading edges), the error in the inferred heating coefficient caused by transverse conduction effects was minimized by acquisition of the data at these early times. The relative intensity phosphor technique does not necessitate corrections for roll-off angle near the planform edges (such as variable emissivity with an infrared thermography technique). As discussed in Ref. 27, the accuracy of the phosphor system measurement is dependent on the temperature rise of the model surface. For the lower-surface (windward) heating measurements the phosphor system measurement accuracy is estimated to be better than $\pm 8\%$, and the overall experimental uncertainty of the phosphor heating data caused by all factors is estimated to be $\pm 15\%$ (including uncertainties in the thermal physical properties of the ceramic material). In areas on the model where the surface temperature rise is only a few degrees (i.e., leeside or flap cavity), the estimated overall uncertainty is on the order of $\pm 25\%$. Repeatability for the normalized windward centerline (laminar) heat-transfer measurements was found to be generally better than $\pm 4\%$.

**Table 3 X-38 aerodynamic reference dimensions**

| Dimension | Full scale (V201) | 0.0175 scale |
|---|---|---|
| $S_{\text{ref}}$ | 233.28 ft$^2$ | 10.288 in.$^2$ |
| $L_{\text{ref}}$ | 27.6 ft | 5.796 in. |
| $b_{\text{ref}}$ $(= L_{\text{ref}})$ | 27.6 ft | 5.796 in. |
| Moment reference center $0.57 \times L_{\text{ref}}$ | 15.732 ft | 3.304 in. |

Based on the analysis of Refs. 27 and 34, the discrete thin-film heat-transfer measurements are estimated to be accurate to within $\pm 8\%$. Repeatability for the cavity heat-transfer measurements was found to be generally better than $\pm 2\%$.

In general, aerodynamic data were obtained in a descending alpha sweep during each run to minimize errors associated with balance heating at the more relevant hypersonic entry angles of attack. In the $CF_4$ facility two separate runs were required to complete an angle-of-attack sweep as a result of the short run time. The data were collected by an analog-to-digital data-acquisition system and averaged over a 1-s interval for each angle of attack (model held at fixed angle of attack for approximately 5 s). The raw data were transferred to a computer for data reduction and storage. During data reduction, corrections for weight tares, sting deflections, and balance interactions were made.

The F&M data measured at the balance electrical center have been transferred to a moment reference center located at 57% of the reference body length along the model $x$ axis. The model OML were checked, and transfer distances were inferred from measurement by the LaRC surface verification laboratory. Table 3 lists the reference area and lengths used to calculate the aerodynamic coefficients.

In the event that anomalous aerodynamic trends were identified, base pressure measurements were made to help assess potential interference effects that might be present because of the sting/support system. Comparisons of measurement with prediction at incidence angles relevant to X-38 hypersonic entry ($\alpha = 40$ deg) suggested little interference, and, as per NASA JSC database requirements, all axial-force coefficients $C_A$ are reported as measured by the force balance (uncorrected for base pressure).

The estimated uncertainty in the reported aerodynamic coefficients was determined and reported[20] using the small sample method presented by Kline and McClintock.[35] Where appropriate, estimated errors in the aerodynamic coefficients are indicated on the figure legend symbols.

**Prediction Methods**

X-38 heating computations for selected angles of attack and test conditions were performed by several organizations within the European computational community. An overview of the computational methodology for X-38 development has been provided in Refs. 14 and 15. All CFD predictions presented in this article were obtained from the X-38 aerothermodynamic database[36] managed by NASA JSC unless otherwise noted. Because of the broad range of CFD codes presently being used to provide wind-tunnel predictions, it was considered impractical to present details associated with surface and volume grid topology, grid-sensitivity studies, and turbulence models in this experimental overview. The reader is referred to Refs. 37–40 for discussion of accuracy associated with the numerical results presented herein.

## Results and Discussion

**Preface**

As an overview of NASA LaRC AB contributions to X-38 aerothermodynamics, this section will highlight some of the more relevant observations to. Details of how the present results are integrated into the JSC/European X-38 design methodology can be found in Refs. 14 and 15. First, the early aerodynamic screening exercises are reviewed and the data compared to the SV-5D preflight database. The influence of Mach number, Reynolds number, and $\gamma$ (real-gas effect) on X-38 hypersonic aerodynamics is discussed. Pitching-moment data have been presented about a moment

reference center located at 57% of the body (reference) length. The aerodynamic results are followed by a synopsis of both global and localized heating measurements including some boundary-layer transition results and an extrapolation of wind-tunnel heating measurements to flight. Flow visualization in the form of surface oil flows is presented to assist in the interpretation of both force and moment and surface heating data. Heating distributions are presented in terms of the ratio of enthalpy based heat-transfer coefficients $h/h_{REF}$, where $h_{REF}$ corresponds to the Fay and Riddell[41] stagnation-point heating to a sphere with radius equal to the X-38 nosecap in the model plane of symmetry. For the global images a constant color-bar maximum value was selected for data presentation (except where noted) to maintain consistency when viewing or comparing the images. On the contour scale the colors tending towards red indicate areas of higher heating (temperatures), whereas the colors towards blue represent areas of lower heating. In areas where the local heating exceeded the selected maximum color-bar value, such as the deflected body flaps or fin leading edges, a gray "overscale" will be evident.

**Aerodynamics**

The initial hypersonic screening conducted in the Mach 20 Helium tunnel focused on the rapid aerodynamic assessment of a modified SV-5D vehicle shape (Rev 3.1) using SLA models. Parametrics were confined to variations of the vehicle leeside and fin leading edges. As expected, no measurable effects on longitudinal aerodynamics at entry angles of attack were observed (not shown). The helium tests were then expanded in scope to evaluate control-surface effectiveness over a range of body-flap deflections and to permit comparison to the PRIME SV-5D preflight wind-tunnel database.[42] (Comparison of the Mach 20 helium aerodynamic coefficients with computational prediction is presented in Ref. 17.) Although real-gas effects on aerodynamics were not simulated in the present laminar Helium test results at Mach 20, the vehicle trim characteristics and $L/D$ are in close agreement with values incorporated into the 1960s database, as shown in Fig. 6. This agreement with the SV-5D database was not surprising as real-gas effects were never quantified and incorporated into the original SV-5D preflight aerodynamic database. From a facility perspective the quantification of real-gas effects on aerodynamic characteristics was in its infancy, and accurate predictive tools were not yet available during the original SV-5D development.

The role of LaRC in X-38 aerodynamic testing was broadened to include tests in other LaRC facilities (e.g., Unitary Plan Wind Tunnel, 16-Foot Transonic Tunnel, and the Low Speed Spin Tunnel) to complement tests conducted in Europe. In the hypersonic regime, the focus of this study, the Rev 3.1 configuration was found to be longitudinally stable, trimming hypersonically at $\alpha = 40$ deg with approximately 15-deg body flaps and a corresponding $L/D = 0.9$. This configuration also exhibited positive directional control across the measured angle of attack range ($10 < \alpha < 50$ deg). The effect of the primary simulation parameters on longitudinal aerodynamics ($C_A$, $C_N$, and $C_m$) was performed by testing of the same model/balance/support system combination in the LaRC LAL. Viscous effects (Reynolds number) associated with a laminar boundary layer were determined at Mach 6. Compressibility effects (Mach number) were determined with comparisons of Mach 6 and 10 air data. Similarly, comparison of aerodynamic measurements between Mach 6 air and $CF_4$ provided an indication of the significance of real-gas effects for X-38 through the variation in normal shock density ratio produced with the two test media.

The effects of Reynolds number on Rev 3.1 longitudinal aerodynamics at Mach 6 for 25-deg body-flap deflection are presented in Fig. 7. Normal-force coefficient (Fig. 7b) remained essentially unchanged over the Reynolds-number range while pitching moment (Fig. 7c) indicated a nose-down increment with increasing Reynolds number. As Reynolds number was increased, it was found that the extent of separated flow on the control surface (as inferred from surface oil-flow visualization; not shown) decreased, as was indicated by the forward movement of the reattachment line on the flap. The presence of flow separation in the vicinity of the deflected control surfaces at all Reynolds numbers suggested a turbulent flow was

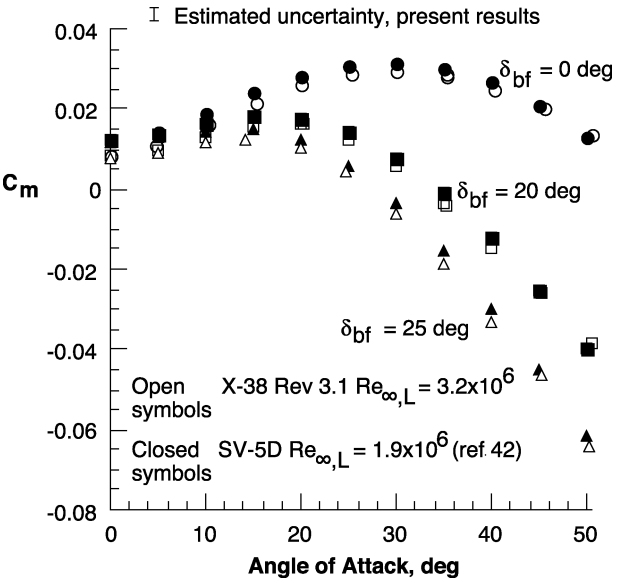


**a) Pitching-moment coefficient: $M_\infty = 20$ helium**

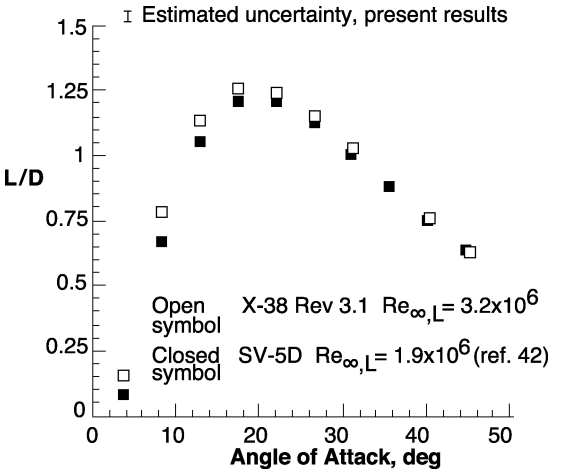


**b) $L/D$: $M_\infty = 20$ helium and $\delta_{BF} = 20$ deg**

**Fig. 6 Comparison of X-38 Rev 3.1 aerodynamics to SV-5D preflight database.**

not obtained at these tunnel conditions, and a limiting case for flap effectiveness was not achieved. (Balance load limits were exceeded at higher Reynolds numbers.) For Mach 6 flight it is anticipated that the boundary layer upstream of the control surfaces will be turbulent, which might further improve flap effectiveness relative to the laminar wind-tunnel results. The decrease in axial coefficient (Fig. 7a) can be attributed to the expected decrease in skin-friction coefficient with increasing Reynolds number for laminar flow conditions. At incidence angles more typical of hypersonic entry, cross-range performance in terms of $L/D$ (not shown) was essentially unaffected over this same laminar Reynolds-number range.

Compressibility effects on Rev 3.1 laminar longitudinal aerodynamics, particularly at hypersonic entry angles of attack, were generally within the experimental uncertainty of the measurements (Fig. 8) with the exception of the Mach 20 axial coefficient (Fig. 8a) obtained in the helium tunnel. The low Mach 20 values of $C_A$ relative to Mach 6 and 10 are more likely caused by the factor of 6 difference in Reynolds number between the Mach 6 and 10 air data and the Mach 20 helium tunnel than a compressibility effect. It is interesting to note a slight crossover in the pitching-moment coefficient (Fig. 8c) between Mach 6 and 10 near $\alpha = 35$ deg. This same trend has been observed both experimentally[43] and computationally[44] within the X-33 program. Although a variety of suggestions[45] have been offered to explain this trend of decreasing stability with decreasing Mach number, a consistent explanation has not been determined.

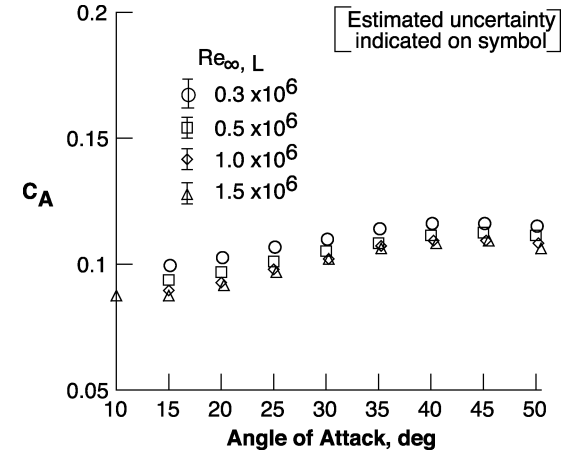


a) Axial-force coefficient

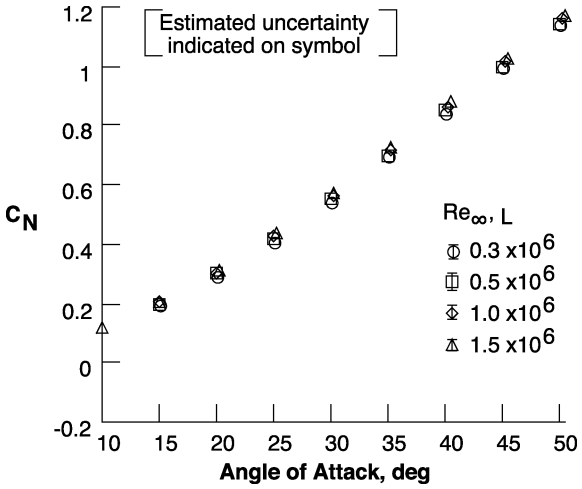


b) Normal-force coefficient

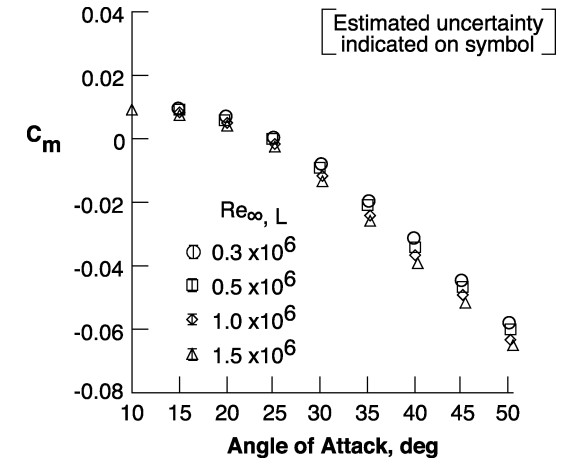


c) Pitching-moment coefficient

**Fig. 7 Reynolds-number effects on X-38 Rev 3.1 longitudinal aerodynamics: $M_\infty = 6$ air and $\delta_{BF} = 25$ deg.**

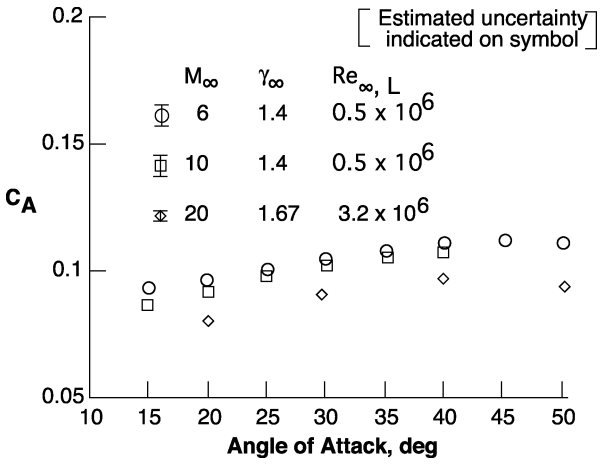


a) Axial-force coefficient

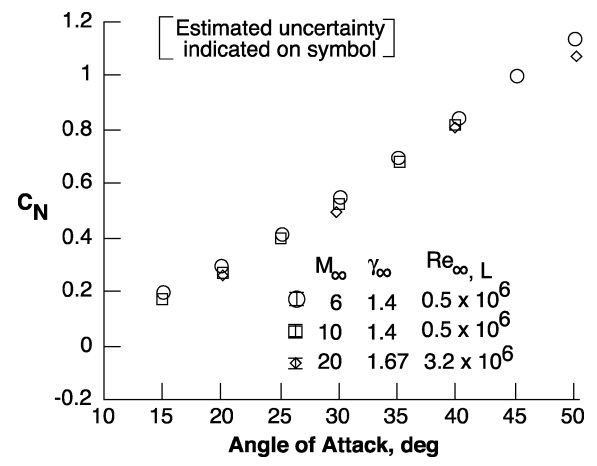


b) Normal-force coefficient

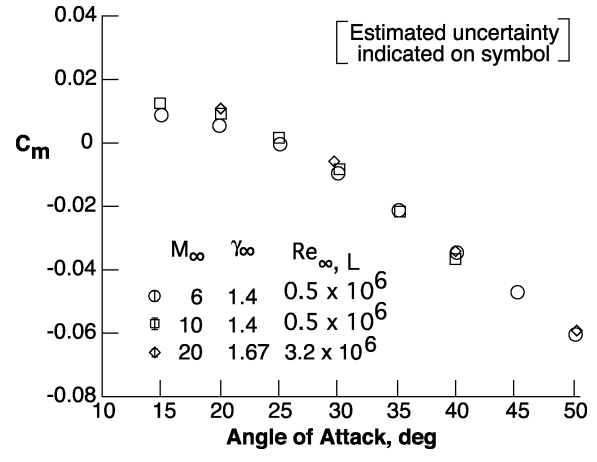


c) Pitching-moment coefficient

**Fig. 8 Mach-number effects on X-38 Rev 3.1 longitudinal aerodynamics: $Re_{\infty,L} = 0.5 \times 10^6$ and $\delta_{BF} = 25$ deg.**

These differences in X-38 $C_m$ at Mach 6 and 10 are within the uncertainty of the measurement, and more than sufficient control authority is produced by the deflected flaps to trim the vehicle.

It was recognized early in the X-38 development phase that real-gas effects were never quantified and incorporated into the original SV-5D preflight aerodynamic database. That is, high-temperature effects caused by dissociation could not be accurately determined (at that time) for the SV-5D basic body pitching moment and body-flap effectiveness. Two decades later, the Space Shuttle Orbiter would experience a significant nose-up pitching-moment increment relative to preflight predictions resulting in body-flap deflections of twice the amount necessary to achieve trimmed flight. This phenomenon was later accurately simulated in the Langley $CF_4$ Tunnel and was coupled with computational methods to provide a high degree of confidence in estimating hypersonic entry aerodynamics.[46] It is commonly recognized today that the primary effect of a real gas on aerodynamics is to lower the specific heat ratio $\gamma$ within the shock layer, which in turn will produce a greater degree of flow compression and expansion relative to a perfect gas. Thus, expansion surfaces will have a correspondingly lower surface pressure. Because of the shuttle experience and the presence of a windward

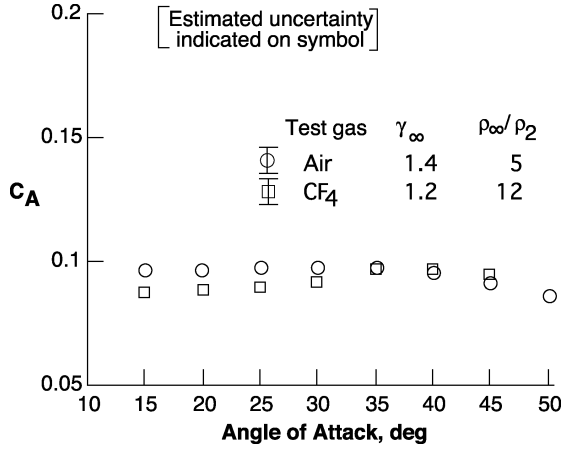


a) Axial-force coefficient

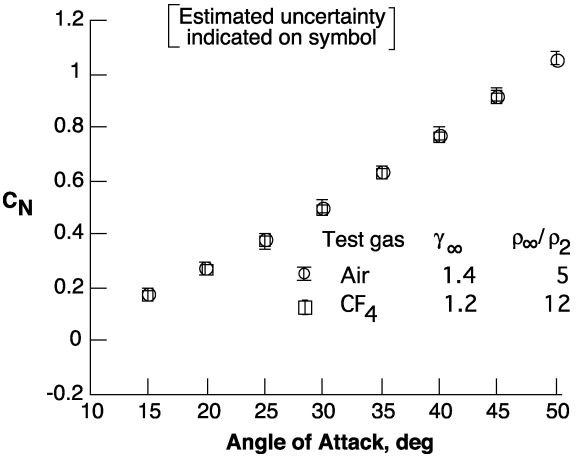


b) Normal-force coefficient

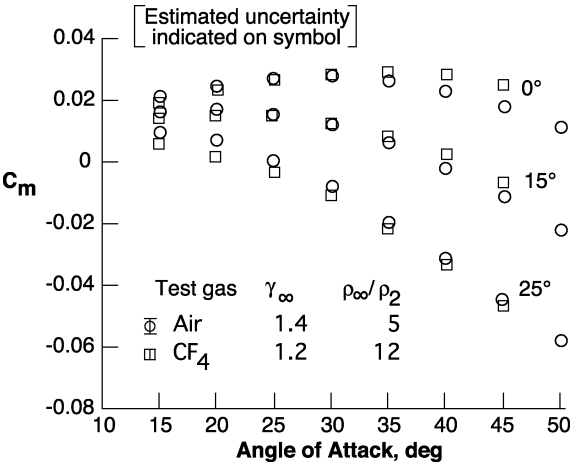


c) Pitching-moment coefficient

**Fig. 9 Gamma $\gamma$ effects on X-38 Rev 3.1 longitudinal aerodynamics: $M_\infty = 6$ $Re_{\infty,L} = 0.25 \times 10^6$ and $\delta_{BF} = 15$ deg.**

expansion surface (boattail) on the aft end of the Rev 3.1 (with the flaps stowed at 0-deg deflection), it was suggested that aerodynamic real-gas simulation testing (similar to that conducted on the orbiter postflight) be performed. The resulting aerodynamic measurements obtained in air and $CF_4$ at identical Mach and laminar Reynolds number (Fig. 9) indicate that testing in a heavy gas ($CF_4$) resulted in small decreases in normal and axial-force coefficients, and a corresponding nose-up pitch increment for a body-flap deflection of 0 deg (Fig. 9c). This trend in the basic body pitching moment (neutral control-surface deflection) was also noted in tests conducted on the orbiter.[46]

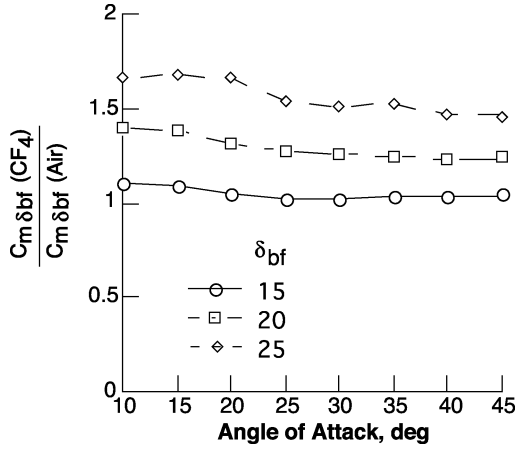


**Fig. 10 Effect of gamma $\gamma$ on X-38 Rev 3.1 body-flap effectiveness: $Re_{\infty,L} = 0.25 \times 10^6$.**

The similarity in real-gas trends between the X-38 and the shuttle ended when the flaps were deployed. With the shuttle the relative nose-up increment between air and $CF_4$ persisted with the body flap deflected for trim.[46] This was not evident from the present X-38 Rev 3.1 test series, which have indicated that for deflections larger than 15 deg a relative nose-down increment in pitching moment was present (Fig. 9c). This is best explained when geometry differences of the respective windward surfaces are recognized. The orbiter has a windward expansion surface that begins and coincides with the largest planform area; deflecting the body flap does not alter the expansion surface as the flap hangs off (trails) the orbiter base. In contrast, the X-38 flap hinge line is located farther forward on the body with the control surfaces deflecting away from the fuselage. Unlike the orbiter, the windward expansion surface (boat-tail) found on the X-38 is effectively eliminated for body-flap deflections greater than 15 deg. Thus, the primary real-gas effects on X-38 aerodynamics at trim conditions are expected to influence flap effectiveness.

Relative to laminar perfect-gas results, the heavy-gas simulation tests revealed an increase in body-flap effectiveness across the angle of attack range (Fig. 10). Real-gas flight computations from Ref. 17 for 25-deg body-flap deflection indicated higher pressure coefficients at the nose and body flap relative to perfect-gas calculations. The pressure increase was more substantial at the flap and affected a larger area, which resulted in a net nose-down increment. Reference 10 indicated that actual flight pressures on the SV-5D boat-tail expansion surface during hypersonic entry were lower than those obtained in wind-tunnel tests and that flight trim flap deflections were less than predicted by the preflight database. The lower flight pressure on the boat-tail surface is consistent with a real-gas effect, and the increased body-flap effectiveness in flight is consistent with trends observed from the present heavy-gas wind-tunnel tests and computational prediction. In general, the increments and trends provided by real-gas simulation tests in air and $CF_4$ are applicable to flight provided that 1) the flight vehicle aerodynamics are dominated by the windward surface, 2) $\gamma$ within the flight windward shock layer does not significantly vary spatially, and 3) $\gamma$ within the flight windward shock layer (near an expansion) is close in magnitude to that produced in $CF_4$ ($\gamma_2 = 1.1$).

Changes to the vehicle outer mold lines continued as the shape was optimized for performance across the speed range. These modifications have been confined to the leeside, and it is assumed that these changes will not result in a significant departure from the real-gas effects already discussed. LaRC facilities have been utilized to assist in the evaluation of these OML changes on aerodynamics from transonic to hypersonic speeds. Tests at Mach 6 conducted on an interim (between Rev 3.1 and 8.3) OML (European designation:YPAIO) revealed marginal lateral stability at lower incidence angles (Fig. 11). In situ model modifications resulted in a laterally stable vehicle across the angle of-attack range. As expected, the addition of an ISS docking mechanism to the vehicle (Rev 8.3)

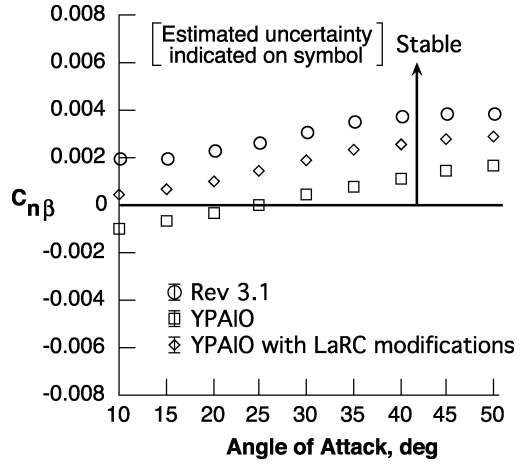


a) Yawing-moment derivative

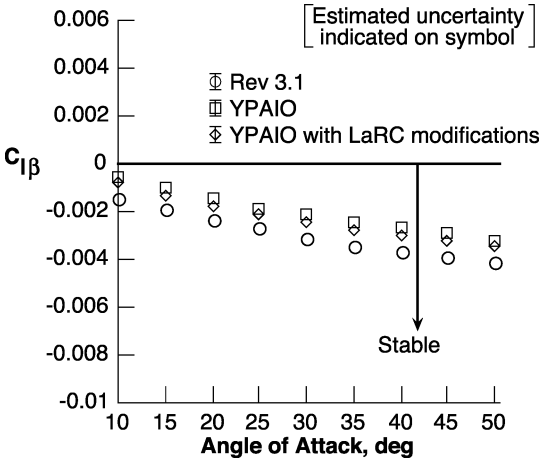


b) Rolling-moment derivative

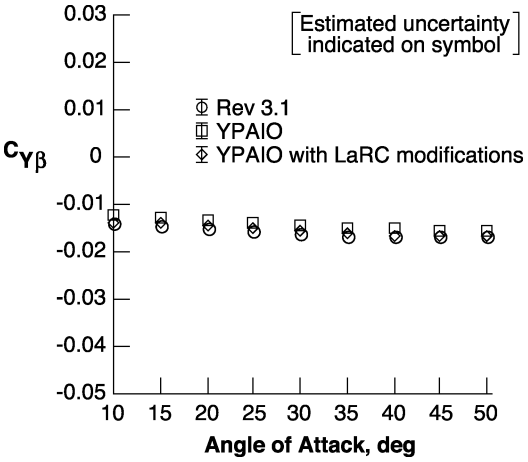


c) Side-force derivative

**Fig. 11 Configuration effects on X-38 lateral/directional aerodynamics: $M_\infty = 6$ air $Re_{\infty,L} = 0.25 \times 10^6$, $\delta_{BF} = 0$ deg, and $\beta = 0 \pm 2$ deg.**

leeside did not produce any measurable effects in the longitudinal or lateral/directional aerodynamics (not shown) at Mach 6 for $15 < \alpha < 50$ deg.

At the time the X-38 was terminated, the program had frozen the OML lines (Rev 8.3) and was focusing efforts on developing and refining an aerodynamic design data book for flight. The X-38 Aerodynamic Data Book[47] (ADB-Rev G) provided a single source reference for all X-38 vehicle data appropriate for full-scale flight performance. Aerodynamic characteristics in the data book up to Mach 10 are based on wind-tunnel tests of various scale models

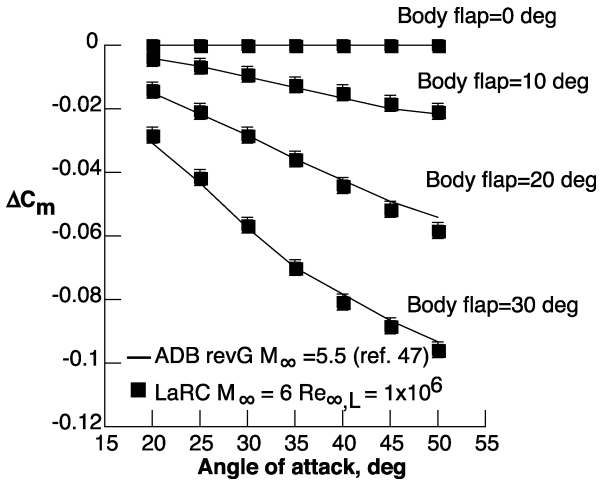


a) $M_\infty = 6$ air

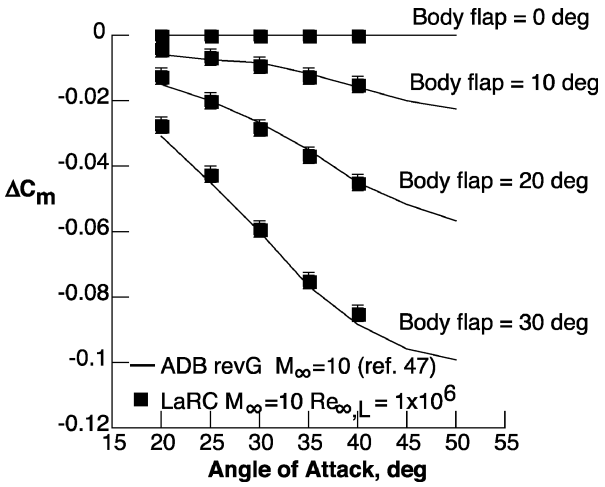


b) $M_\infty = 10$ air

**Fig. 12 Comparison of X-38 Rev 8.3 pitching-moment increments with X-38 preflight ADB-Rev G.**

tested in Europe. (From Mach number of 10 to rarified conditions, aerodynamic data are based on CFD predictions.[47]) Included in the book are aerodynamic body-flap control effectiveness data across the Mach range, which are presented in terms of increments from an undeflected state. Laminar body-flap pitching-moment increments $\Delta C_m$ from LaRC tests at Mach 6 and 10 at a length Reynolds number of $1 \times 10^6$ are presented in Fig. 12a, along with the current ADB (Rev G) values. Differences between the LaRC results and the ADB (Rev G) are small and are within the uncertainties that would have been allowed for by the X-38 flight control system.

### Windward Surface Heating

Flight surface heating data from the SV-5D Precision Recovery Including Maneuvering Entry (PRIME) project of sufficient quality and quantity are not available for X-38 TPS design. The primary objective of the PRIME program was to demonstrate, through flight testing, lifting-body aerodynamic performance during hypersonic entry at cross ranges up to 700 miles. With the emphasis placed on aerodynamics, the flight program did not attempt to produce a large flight heating database.[48] (Heating over most of the body was inferred from flight pressure measurements.) Ground tests conducted at the time proved to be sufficiently accurate for a conservative heat-shield design.[11] Lightweight ablative materials were used over the entire surface as anticipated heating conditions were considered to be more extreme than those expected for larger operational vehicles (such as the shuttle flown almost 20 years later).

In terms of experimental and predictive methods, the aerothermodynamic community has progressed considerably since the

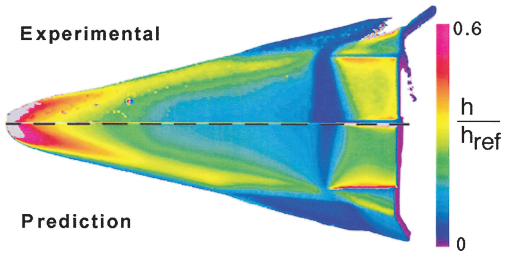


**Fig. 13 Comparison of measured X-38 Rev 3.1 global windward heating with laminar prediction[17]: $M_\infty$ = 10, $\alpha$ = 40 deg, $\delta_{BF}$ = 25 deg, and $Re_{\infty,L} = 0.5 \times 10^6$.**

development of the SV-5D vehicles. Up until the mid-1990s, however, experimental aeroheating information for configuration assessment had continued to lag behind aerodynamic information because primarily of model and instrumentation complexities associated with aerothermodynamic testing. The X-38 program was able to take advantage of recent developments in the two-color global phosphor thermography technique, providing an opportunity to conduct an aerothermodynamic screening/trade study concurrent with aerodynamic tests. The aeroheating measurements from LaRC were primarily used in the continued development and validation of computational tools used to predict the X-38 aeroheating environment. Similar to the aerodynamic methodology of the program, the LaRC aerothermal results were also intended to duplicate or compliment test results obtained in European facilities.

Figure 13 illustrates a typical global comparison between experimental and numerically predicted laminar heating[17] at wind-tunnel conditions. The comparisons suggest a high level of confidence in the laminar numerical simulation over the acreage of the windward surface where the flow remains attached. Differences in the magnitude of the deflected flap surface heating and the apparent size of the separated flow upstream are indicative of a flow complexity that is more challenging to simulate numerically. Extracted heating distributions for this condition near the windward centerline and at two axial stations are presented in Fig. 14 and are compared to a laminar General Aerodynamic Simulation Program (GASP) prediction.[17] Measured centerline SV-5D heating data[49] from wind-tunnel tests conducted at Arnold Engineering Development Center (AEDC) Tunnel C at Mach 10 and the Martin Hot Shot tunnel at Mach 20 over 35 years ago are also shown with the present LaRC Mach 10 results and prediction in Fig. 14a. Differences between the SV-5D data sets were noted at that time[49] but were never resolved. (Although state of the art at the time, the large uncertainties in the SV-5D data are presumed to be caused by the nature of the thin-skin calorimetry test technique.) The SV-5D data sets bracket the present Mach 10 experimental and computational results. In retrospect, the experimentally determined SV-5D heating environment was adequate for a conservative TPS design. Modern quantitative global capabilities (experimental and computational) that are available today provide orders of magnitude more information in a fraction of the time permitting a less conservative design.

Although primarily intended to provide data for computational validation, the LaRC tests were also intended to assess quantitatively the effects of Reynolds number, angle of attack, boundary-layer transition, and configuration changes on heating. Subsonic/transonic aerodynamic optimization did lead to leeside OML changes, and as a result some effort was devoted to the assessment of these changes on the heating environment. No significant issues regarding leeside heating (i.e., canopy, docking ring, or aft base flare) were identified experimentally.

On the windward surface the influences of Reynolds number were most pronounced in the vicinity of the deflected flaps. Rev 3.1 windward heating at $M_\infty = 6$, $\alpha = 40$ deg, and body-flap deflection = 25 deg are presented in Fig. 15 for a range of Reynolds number. The extracted longitudinal distributions are taken just off centerline so as to capture the flap heating trends. (Heating to the cavity floor between the flap-split gap will be discussed later.) The collapse of the heating distributions with Reynolds number upstream

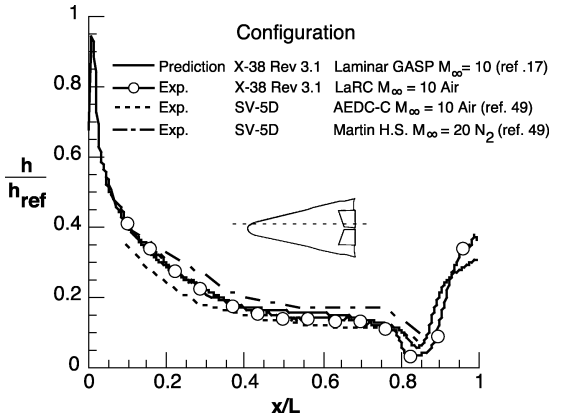


**a) Windward centerline**

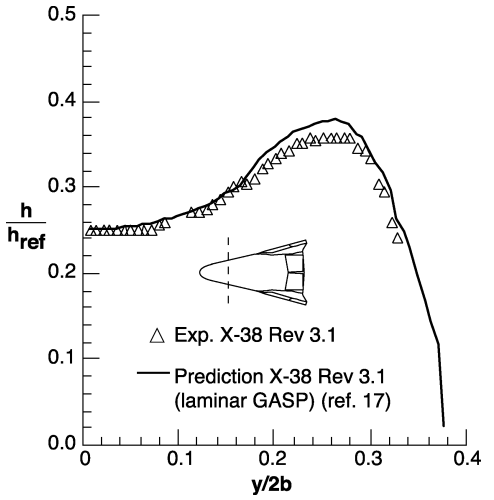


**b) Axial station, $x/L$ = 0.25, $M_\infty$ = 10 air**

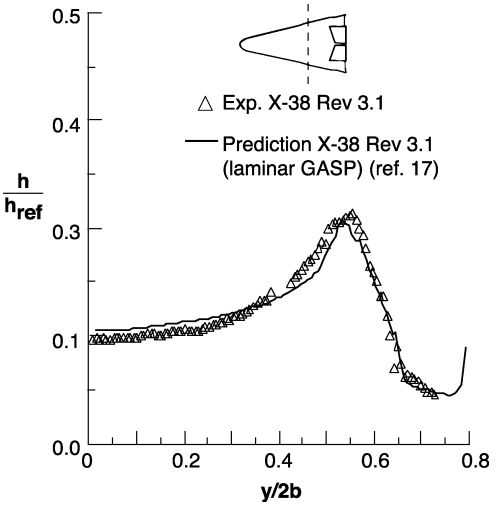


**c) Axial station, $x/L$ = 0.73, $M_\infty$ = 10 air**

**Fig. 14 Comparison of measured X-38 Rev 3.1 and SV-5D heating distributions with laminar prediction: $M_\infty$ = 10, $\alpha$ = 40 deg, $\delta_{BF}$ = 25 deg, $Re_{\infty,L} = 0.5 \times 10^6$.**

of flap flow separation indicated the approaching flow was laminar. The corresponding windward global heating images and surface streamline patterns are shown in Figs. 16 and 17, respectively. Consistent with conclusions inferred from the aerodynamic results, the extent of flow separation diminished with increasing Reynolds number. The flow reattachment downstream on the flap was observed to be in close proximity and nearly parallel to the 10-deg inboard swept-flap hingeline. The flap hingeline gap was designed with a seal to prevent circulation of this high-energy flow into the cavity.

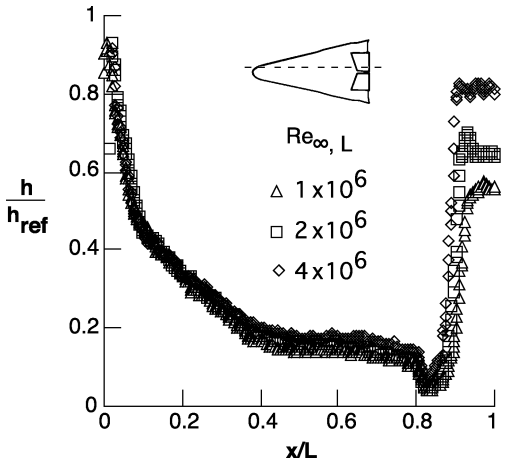


**Fig. 15 Effect of Reynolds number on Rev 3.1 windward centerline heating distribution: $M_\infty$ = 6 air, $\alpha$ = 40 deg, and $\delta_{BF}$ = 25 deg.**

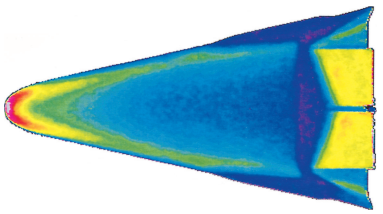

a) $Re_{\infty,L} = 1 \times 10^6$

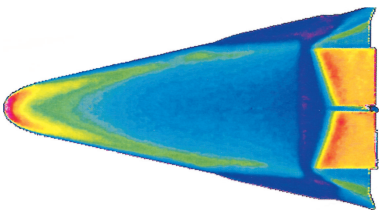

b) $Re_{\infty,L} = 2 \times 10^6$

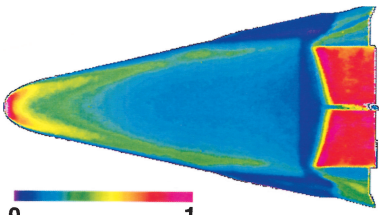


c) $Re_{\infty,L} = 4 \times 10^6$

**Fig. 16 Effect of Reynolds number on Rev 3.1 global windward heating: $M_\infty$ = 6 air, $\alpha$ = 40 deg, and $\delta_{BF}$ = 25 deg.**

Near flap reattachment the streamlines are highly three dimensional; inflow towards the flap split gap and expansion over the outboard flap edge was evident over the range of Reynolds numbers and at all angles of attack. The variation of heating levels on the flap with Reynolds number suggested a transitional/turbulent flow reattachment process. Flap heating will be discussed in more detail in a subsequent section.

### Fin/Rudder Heating

The circulation of separated flow upstream of flap reattachment appeared to result in outboard flow spillage onto the nearby fin. Rev 8.3 heating images in Fig. 18 obtained at Mach 6 on the fuselage side ($\alpha = 40$ deg, body-flap deflection $= 20$ deg) indicated possible boundary-layer transition of this entrained flow up onto the rudder surface. A comparison of extracted data along the fin chord in the

a) $Re_{\infty,L} = 1 \times 10^6$

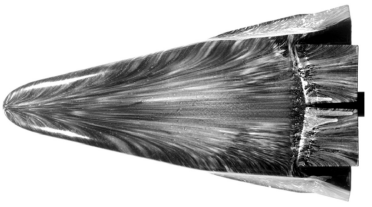

b) $Re_{\infty,L} = 2 \times 10^6$

c) $Re_{\infty,L} = 4 \times 10^6$

**Fig. 17 Effect of Reynolds number on Rev 3.1 windward surface streamlines: $M_\infty$ = 6 air, $\alpha$ = 40 deg, and $\delta_{BF}$ = 25 deg.**

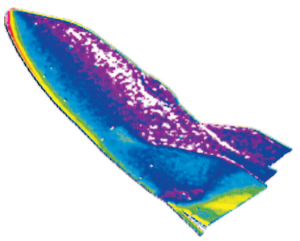

a) $Re_{\infty,L} = 1 \times 10^6$

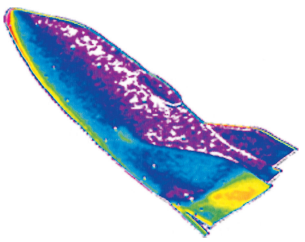

b) $Re_{\infty,L} = 2 \times 10^6$

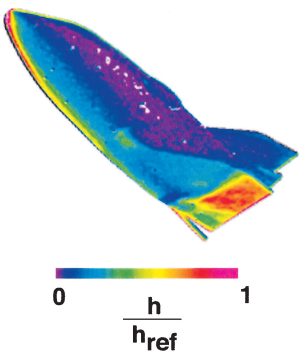


c) $Re_{\infty,L} = 4 \times 10^6$

**Fig. 18 Effect of Reynolds number on Rev 8.3 fin/rudder global heating: $M_\infty$ = 6 air, $\alpha$ = 40 deg, and $\delta_{BF}$ = 20 deg.**

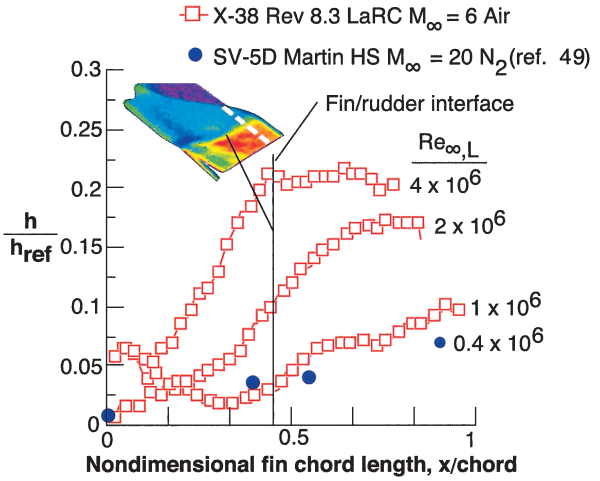


**Fig. 19 Effect of Reynolds number on X-38 Rev 8.3 fin/rudder heating distribution and comparison with SV-5D: $M_\infty$ = 6 air, $\alpha$ = 40 deg, and $\delta_{BF}$ = 25 deg.**

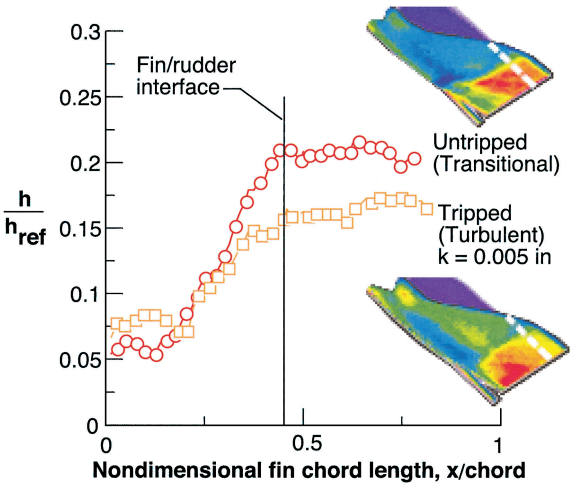


**Fig. 20 Effect of Reynolds number on X-38 Rev 8.3 fin/rudder chordwise heating distribution: $M_\infty$ = 6 air, $\alpha$ = 40 deg, $Re_{\infty,L} = 4 \times 10^6$, and $\delta_{BF}$ = 25 deg.**

vicinity of the rudder from the present tests with data from Ref. 49 is shown in Fig. 19. Boundary-layer transition in the present tests has been inferred from the heating increase observed on the fin with increasing Reynolds number. Transitional/turbulent flow on the fin was not reported from the Mach 20 wind-tunnel test supporting the SV-5D development[49] and was likely caused by boundary-layer stabilization at high Mach number and low Reynolds number. Tripping of the fin boundary layer with discrete roughness elements placed along the windward chine area suppressed the measured fin heating from transitional to turbulent levels as shown in Fig. 20. When present, transitional heating on the fin rudder is four or more times the laminar value.

A comprehensive numerical analysis of the heating in the rudder/fin gap[50] has indicated that a seal (or alternatively, an ablator material) might be required. In Ref. 50 it was shown that high heating on the rudder occurred at Mach 17.5 and 11, which conservatively assumed laminar and turbulent flow over the fin, respectively. The heating implications of transitional or turbulent flow near the fin rudder at $M_\infty = 17.5$ have not been fully assessed.

### Windward Flap Heating

The thermal environment associated with the X-38 body flaps is considered to be a challenge from a design perspective caused by the complex three-dimensional flowfield and resulting high surface temperatures anticipated in flight. The windward flap temperatures in flight will be driven by several factors: three-dimensional flow

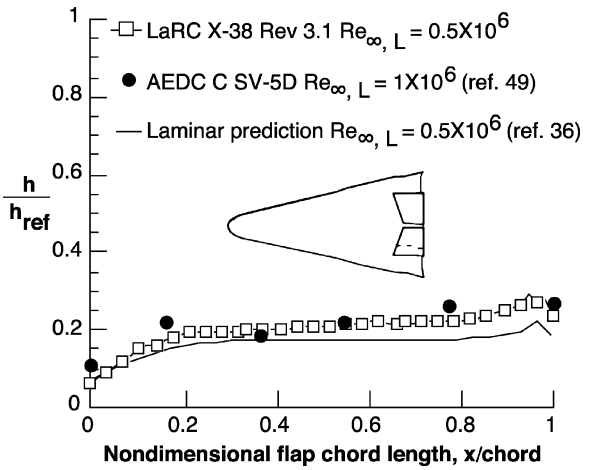


**Fig. 21 Comparison of measured X-38 Rev 3.1 and SV-5D body-flap heating distribution with laminar prediction: $M_\infty$ = 10 air, $\alpha$ = 40 deg, and $\delta_{BF}$ = 20 deg.**

separations, shear-layer transition, multiple shock processing of the flow (bow, separation, reattachment), and flow expansion and acceleration over the flap edges and through the split gap. The X-38 flaps are designed as a hot structure[51] and will be manufactured from C/SiC, a ceramic matrix composite[52] (CMC). Early estimates of flap thermal loads suggested that CMC technology could provide an adequate thermal margin; however, vehicle weight growth and trajectory refinements have significantly reduced this margin. A comprehensive computational and experimental effort has been initiated to more accurately predict the heating environment associated with the windward surface of the deflected body flaps and to ensure this margin is not exceeded.

The peak heating to the deflected body flaps is largely determined by the state of the separated flow as it reattaches on the control surface. Three situations can arise: 1) laminar separation with laminar reattachment, 2) laminar separation with transitional or turbulent reattachment, or 3) turbulent separation with turbulent reattachment. (It should be noted that turbulent flow approaching the flap might eliminate flow separation.) Comparison of the early LaRC Mach 10 heating extracted along the Rev. 3.1 flap chord near the centerline ($\alpha = 40$ deg, flap deflection of 20 deg) with laminar SV-5D data from Ref. 49 and laminar Navier–Stokes prediction[36,40] from the CEVCATS code[53] is presented in Fig. 21. The agreement with the experimental data from Ref. 49 is noteworthy considering the state of the art in instrumentation, signal conditioning, and data reduction in the 1960s. The laminar Navier–Stokes solution underpredicted the measured flap heating, which has suggested that either the numerical simulation of the laminar flow separation and reattachment process was inadequately modeled, or that nonlaminar conditions prevailed in the Mach 10 ground tests. Recent testing at Mach 10 with smaller scale Rev 8.3 heating models has suggested that laminar conditions were achieved at and downstream of flap reattachment.[54]

Laminar flap heating on the initial 10 in Rev. 3.1 models was not identified at Mach 6 for all Reynolds number conditions, and it is believed that the flap heating was indicative of transitional or turbulent flow reattachment. (A laminar interaction was later inferred from heating measurements made on 6 in Rev. 8.3 models[54] tested at Mach 6 at lower Reynolds numbers.) The LaRC X-38 Rev 3.1 and 8.3 data were instrumental in developing flap heating correlations and flight scaling factors for separating laminar, transitional, or turbulent flows. The effects of flap deflection on Rev 3.1 global heating images obtained at Mach 6, $\alpha = 40$ deg, and $Re_{\infty,L} = 2 \times 10^6$ are shown in Fig. 22. Extracted flap span heating distributions ($X/L = 0.98$) are presented in Fig. 23. The heating distributions along the body fuselage and flap chord ($y/b = 0.2$) are shown in Fig. 24 and correspond to the deflections shown in Fig. 23. The images at these conditions (as well as all others) did not reveal the presence of Gortler vortices as is sometimes evident downstream

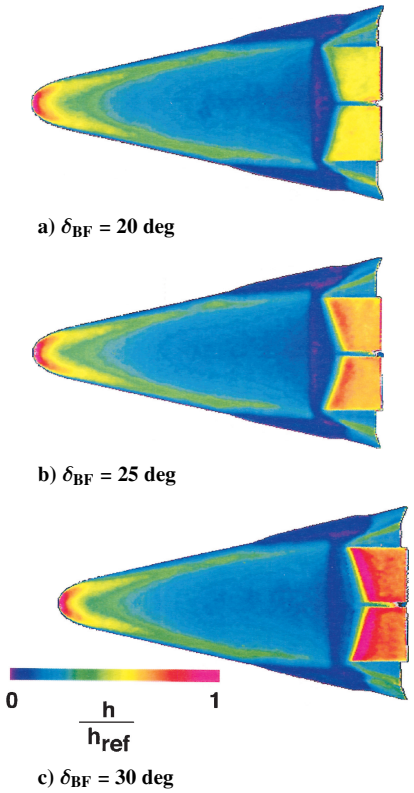


**Fig. 22 Effect on body-flap deflection on Rev 3.1 global windward heating: $M_\infty = 6$ air, $\alpha = 40$ deg, and $Re_{\infty,L} = 2.0 \times 10^6$.**

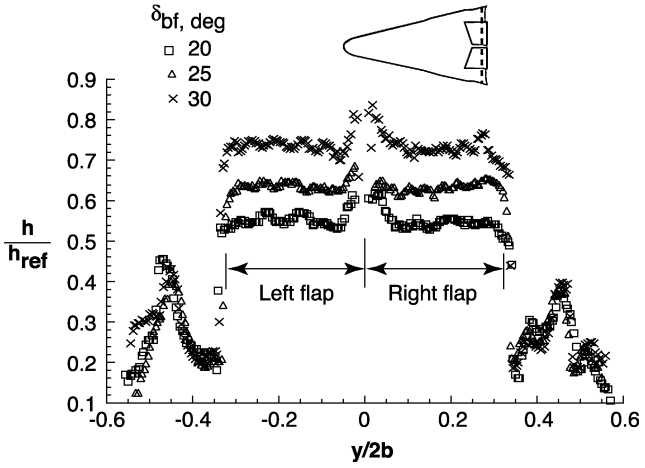


**Fig. 23 Effect on body-flap deflection on Rev 3.1 flap span heating distribution at $x/L = 0.98$, $M_\infty = 6$ air, $\alpha = 40$ deg, and $Re_{\infty,L} = 2.0 \times 10^6$.**

of flow reattachment. This type of flow instability can produce heating augmentations of 30–50% above turbulent values[55] and was a major issue in the thermal design specifications of the flap.[56] In the present studies it is felt that the resolution of the phosphor camera would not have detected the heating striation associated with the short-wavelength boundary-layer vortices if they were present on the X-38 flap. Futhermore, it has been debated as to whether Gortler-type vortices can be sustained in a highly unsteady turbulent flow.[55]

Extracted heating distributions along the flap span near the trailing edge (Fig. 23) were constant with the exception of the area near the flap split gap. An approximate heating increase of 15% to the flap edge was measured and is the result of the inflow toward the gap (and inferred acceleration over the edge) observed in the streamline patterns presented earlier (Fig. 17). Increasing the body-flap deflection angle from 20 to 30 deg resulted in a 40% increase

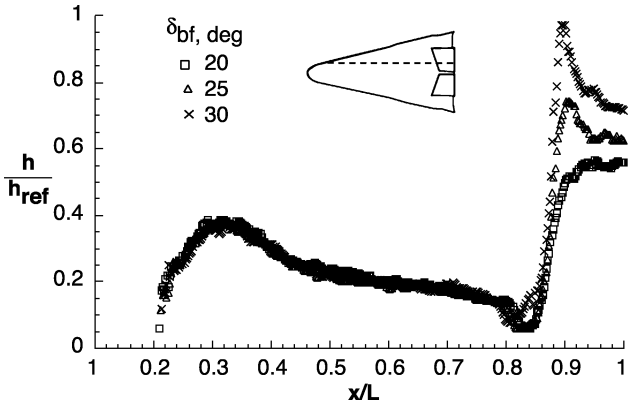


**Fig. 24 Effect on body-flap deflection on Rev 3.1 longitudinal heating distribution at $y/2b = 0.2$, $M_\infty = 6$ air, $\alpha = 40$ deg, and $Re_{\infty,L} = 2.0 \times 10^6$.**

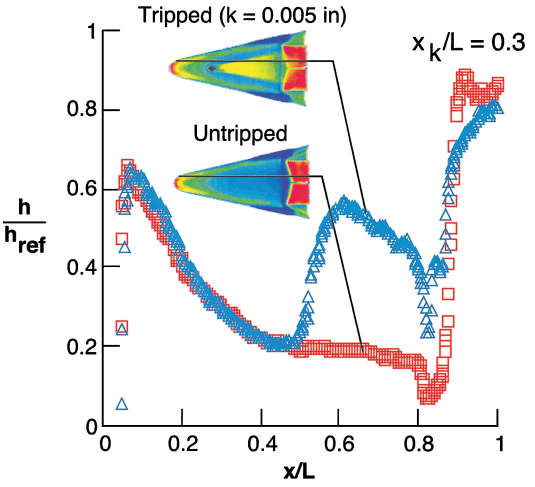


**Fig. 25 Effect of boundary-layer trip on X-38 Rev 3.1 longitudinal body-flap heating distribution: $M_\infty = 6$ air, $\alpha = 40$ deg, $Re_{\infty,L} = 4 \times 10^6$, and $\delta_{BF} = 25$ deg.**

in overall heating levels on the flap downstream of reattachment. Closer to the point of flow reattachment ($X/L = 0.9$), flap deflection had a more pronounced effect on heating, as shown in Fig. 24. The "overshoot" in heating at reattachment for body-flap deflections of 25 and 30 deg can be characteristic of transitional flow. As observed with the fin heating, turbulence forced with discrete roughness elements placed upstream of separation reduced the extent of separation and suppressed the measured transitional heating on the flap at $Re_{\infty,L} = 4 \times 10^6$ (Fig. 25). The suppression of reattachment heating on the flap relative to transitional levels was also consistent with results obtained from heating studies conducted at AEDC on the SV-5D[57] (not shown).

Numerical prediction of transitional and turbulent interactions, such as that which occurs with the X-38 deflected flap, remains challenging. Turbulence models play a crucial role in the simulation of complex flows where separation, shock/boundary-layer interaction, and flow reattachment are present. The correct prediction of surface heating magnitude and distribution depends to a large degree on the turbulence model used. Predicted laminar and turbulent body and flap heating distributions[36] from the CFD codes detailed in Refs. 53, 58, and 59 were compared to the measured LaRC Mach 6 heating data to develop a higher degree of confidence in predictive techniques utilized for X-38 flap design. The experimental heating distributions presented in Fig. 26 ($\alpha = 40$ deg, body flap $= 20$ deg, and $Re_{\infty,L} = 4 \times 10^6$) correspond to laminar and turbulent flow upstream of the deflected flap. The predicted laminar heating distributions from the two Navier–Stokes solvers[53,58,59] and a two-layer (Euler plus boundary-layer) method[59] agreed with measured values and indicated the boundary layer upstream of flow separation was

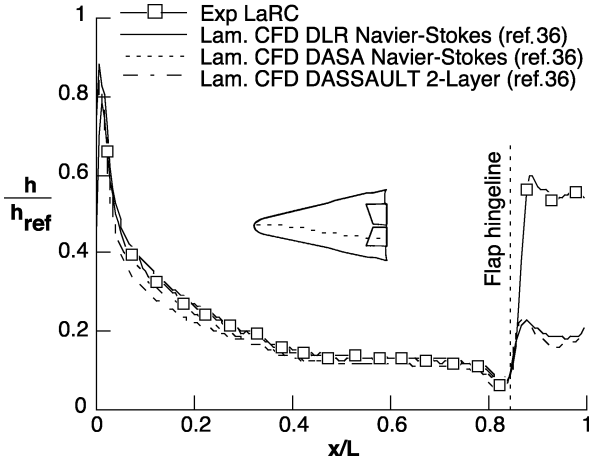


a) Laminar

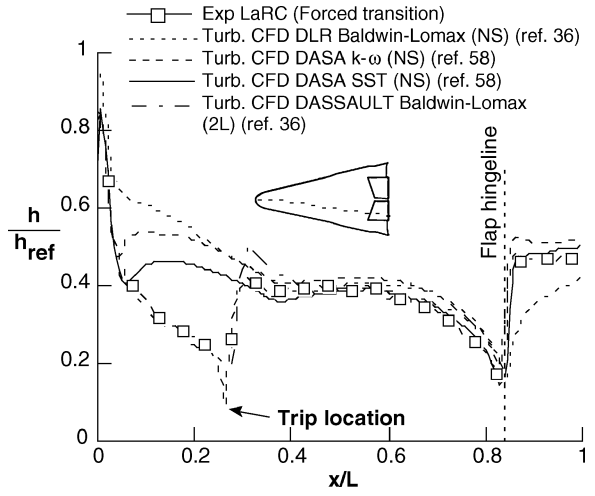


b) Turbulent

**Fig. 26 Comparison of measured X-38 Rev 8.3 body and flap longitudinal heating distribution with prediction: $M_\infty$ = 6 air, $\alpha$ = 40 deg, $Re_{\infty,L} = 4 \times 10^6$, $\delta_{BF}$ = 20 deg.**

laminar (Fig. 26a). On the deflected flap the measured heating was a factor of three higher than laminar predictions, which suggested a nonlaminar flow reattachment. (The two-layer method was not used to predict flap heating.) Experimentally, the boundary layer was forced turbulent via discrete roughness and the resulting heating distribution compared to turbulent prediction[53,58,59] (Fig. 26b). As expected, the algebraic Baldwin–Lomax turbulence model[59] did not perform well in the vicinity of the flap where an adverse pressure gradient and flow separation exist. A modified two-equation ($k$–$\omega$) turbulence model[58] more accurately predicted the heating magnitude on the flap. The shear stress transport (SST) turbulence model most closely reproduced the measured heating distribution on the deflected flap. Although this comparison does not imply that the turbulence model has been validated for flight, it does suggest that of the three numerical models investigated the SST might be the most suitable for application to X-38 flap design. Reference 58 provides a detailed discussion of the numerical turbulence models and comparisons to additional LaRC X-38 data and other benchmark experiments.

### Flap Cavity Heating

The aerothermal environment of the cavity located behind the deflected flaps represents an extreme challenge from an experimental and numerical modeling perspective. In flight, forced convection through the flap gap, radiative heating between the flap leeside and aft cavity surfaces, flow separation, and flow three-dimensionality are all present. The presence of critical component hardware such

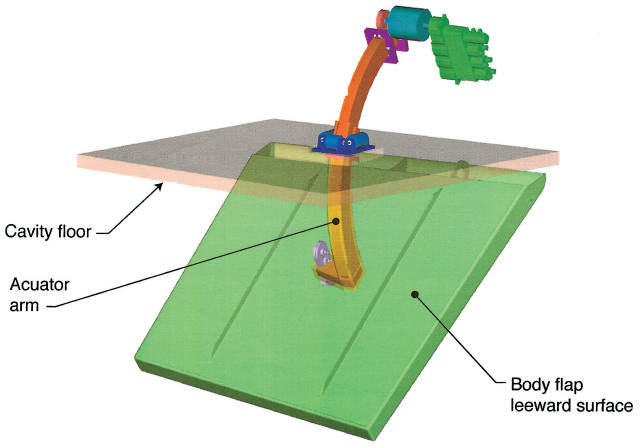


**Fig. 27 X-38 Rev 8.3 flap cavity and actuator arm location (second flap omitted for clarity).**

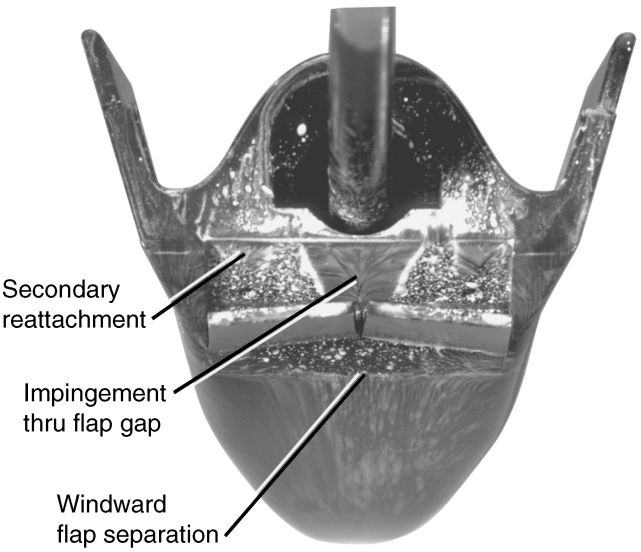


**Fig. 28 X-38 rev 8.3 surface streamlines on flap cavity floor: $M_\infty$ = 6 air, $\alpha$ = 40 deg, $Re_{\infty,L} = 2.0 \times 10^6$, and $\delta_{BF}$ = 20 deg.**

as the flap actuator rod (Fig. 27) requires an accurate prediction of the environment to ensure proper performance and adequate thermal protection. Experimentally, the cavity flowfield behind the flaps was dominated by the jet-like impingement of the flow through the flap split gap onto the cavity floor. A photograph of the surface streamline patterns on the cavity floor from flow impingement at Mach 6, $\alpha = 40$ deg, body flap = 20 deg is shown in Fig. 28. The impingement produced longitudinal and spanwise variations in surface shear on the cavity floor. Comparison of the streamline patterns shown in Fig. 28 to those obtained on a model with a leeward blade-mounted support system (see Fig. 5a) suggested interference effects within the cavity region from a base-mounted support sting were not present.

To characterize the heating from the jet-like impingement, NASA LaRC provided the first detailed convective heating measurements made on the X-38 cavity surface. A comparison of Navier—Stokes laminar and turbulent cavity heating prediction[36] from the CFD code detailed in Ref. 58 is shown in Fig. 29 at wind-tunnel conditions ($\alpha = 40$ deg, body flap = 20 deg, and $Re_{\infty,L} = 4 \times 10^6$). For comparative purposes the global heating prediction on the cavity floor to the left of the symmetry plane corresponds to turbulent flow using a two-equation ($k$–$\omega$) turbulence model and to the right of the symmetry plane, laminar flow. From a predictive standpoint the assumed state of the flow within the cavity had little effect on the surface heating magnitude and distributions. In Fig. 29 the global heating predictions are contrasted with cavity floor heating measurements

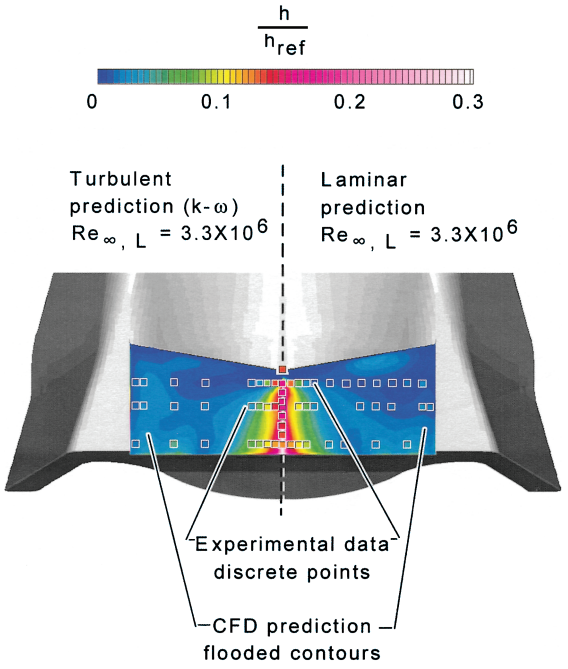


**Fig. 29 Comparison of discrete thin-film experimental cavity floor heating with laminar and turbulent prediction[36]: $M_\infty$ = 6 air, $Re_{\infty,L}$ = 4 × 10$^6$, and $\delta_{BF}$ = 20 deg.**

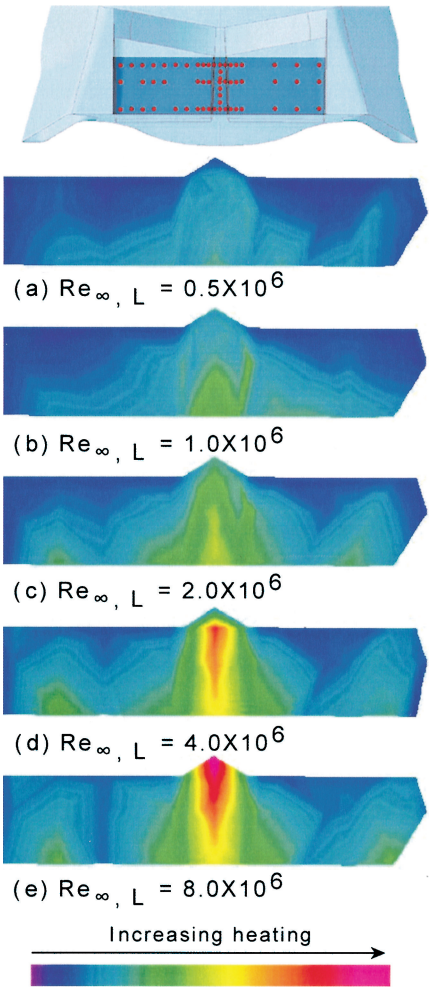


**Fig. 30 Effect of Reynolds number on X-38 Rev 8.3 measured cavity floor heating: $M_\infty$ = 6 air, $\alpha$ = 40 deg, and $\delta_{BF}$ = 25 deg.**

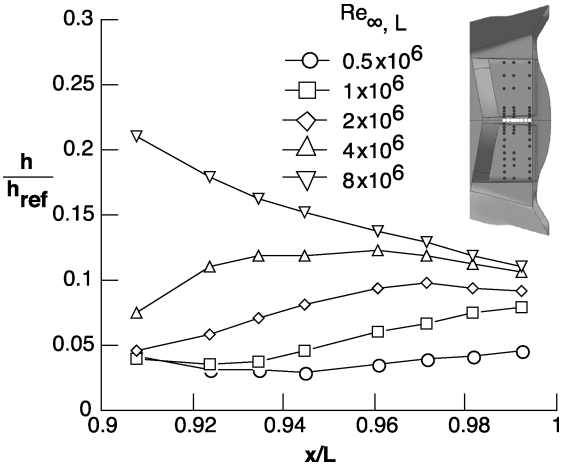


**Fig. 31 Effect of Reynolds number on X-38 Rev 8.3 centerline cavity floor heating distribution: $M_\infty$ = 6 air, $\alpha$ = 40 deg, and $\delta_{BF}$ = 25 deg.**

made at discrete locations (designated by square symbols). The heating magnitudes from the discrete thin-film measurements have been assigned color contour levels (indicated within square symbol) corresponding to that used for prediction. Similar to the phosphor results, the warmer colors (yellow, red, etc.) correspond to areas of higher heating. With the exception of the location of the predicted cavity heating peak between the flap gap, the numerical solutions captured the surface heating characteristics measured on the cavity floor. At this Reynolds-number condition ($Re_{\infty,L} = 4 \times 10^6$) it was determined experimentally that the measured heating peak to the cavity surface was located on centerline near the flap hingeline. In contrast, the computationally predicted heating peak on the cavity floor was located near the vehicle trailing edge.

Additional experimental tests revealed that the heating peak to the cavity floor exhibited a strong spatial sensitivity to Reynolds number not predicted computationally. To visually capture global heating characteristics of the cavity floor from the discrete thin-film measurements, the data obtained at Mach 6, $\alpha = 40$ deg, body flap = 25 deg are interpolated and presented in the form of a color contour plot in Fig. 30. The forward movement of the heating peak toward the flap hingeline with increasing Reynolds number was observed. Secondary heating peaks were measured outboard of the centerline near the cavity vertical side wall and corresponded to vortical flow inferred from the increase in shear in the surface streamline pattern shown in Fig. 28. The same data are replotted in a more conventional format, whereby centerline cavity normalized heating distributions are plotted vs vehicle length ($X/L$) (Fig. 31). In the wind tunnel the range of length Reynolds numbers was sufficient to produce laminar and turbulent flow on the flap windward surface. The increase in magnitude and forward movement of the heating maximum on the cavity floor with increasing Reynolds number coincided with the forward movement of flow reattachment (decreasing separation) on the windward flap surface. The magnitude increase and shift of the heating maximum with Reynolds number in the present Mach 6 tests were consistent with Mach 10 trends obtained from heating studies conducted at AEDC on the SV-5D.[57] (This trend was observed with extreme flap deflections of 40 deg.) A direct comparison of the SV-5D cavity centerline Mach 10 data of Ref. 57 with the corresponding LaRC Mach 6 X-38 heating distribution was possible for a flap deflection of 20 deg and is shown in Fig. 32. Although the data from Ref. 57 were spatially limited (two thermocouples on the cavity floor), the heating maximum appears to have been located near the aft end of the vehicle. This is consistent with the present Mach 6 trends observed at low Reynolds number. The opening of a hingeline flap seal on the wind-tunnel model of Ref. 57 appeared to shift the cavity heating maximum forward towards the flap/cavity interface. Relief of the separated flow on the flap windward surface through the gap would appear to have produced a smaller recirculation region, emulating the high-Reynolds-number Mach 6 cavity heating trends from the present test. Additional tests at higher

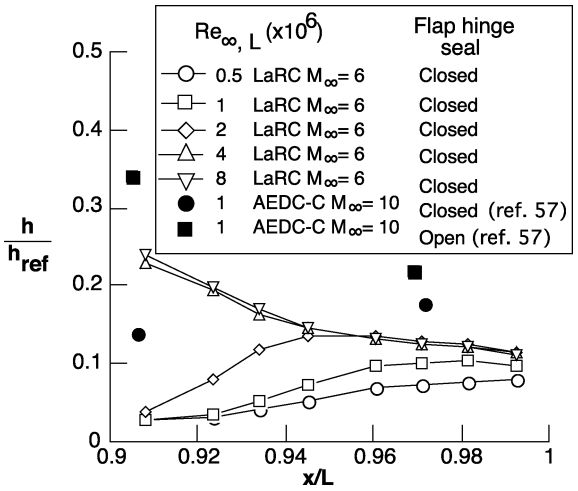


**Fig. 32 Comparison of measured X-38 Rev 8.3 and SV-5D centerline cavity floor heating distribution: $M_\infty$ = 6 air, $\alpha$ = 40 deg, and $\delta_{BF}$ = 20 deg.**

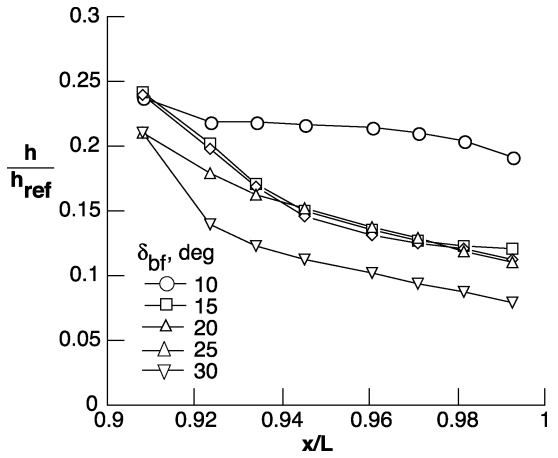


**Fig. 33 Effect of body-flap deflection on X-38 Rev 8.3 centerline cavity floor heating distribution: $M_\infty$ = 6 air, $\alpha$ = 40 deg, and $Re_{\infty,L} = 8 \times 10^6$.**

Mach number ($M > 6$) are required to determine whether differences in the heating magnitude from the present test and Ref. 57 are caused by compressibility effects. At high-Mach-number equilibrium conditions experienced during actual hypersonic entry, the location of peak heating on the cavity floor might not be as sensitive to Reynolds number as that inferred from the Mach 6 perfect-gas wind-tunnel environment. As observed in Ref. 46, the predicted region of separated flow on the shuttle flap windward surface was smaller at equilibrium flight conditions than for the corresponding Mach 6 perfect-gas wind-tunnel case. Based on the available data, it is reasonable to assume that a smaller separated region in flight for the X-38 would limit movement of the cavity floor heating peak with Reynolds number relative to that observed with the present perfect-gas measurements. Differences in the X-38 control-surface shock system (flap shock and separation shock) between equilibrium flight and the Mach 6 perfect-gas wind-tunnel case would also process the gas entrained between the flaps differently and would ultimately affect the cavity floor heating magnitude as well.

The effect of angle of attack and body-flap deflection on cavity heating is presented in Figs. 33 and 34. Turbulent conditions on the flap windward surface prevail at this Reynolds number in the wind tunnel ($Re_{\infty,L} = 8 \times 10^6$) and are anticipated in flight at Mach 6. In contrast to the decreased heating on the windward flap surface, the lower flap deflections produced a more severe thermal environment on the cavity floor (Fig. 33). The effect of angle of attack on cavity heating at $Re_{\infty,L} = 8 \times 10^6$ for a fixed flap deflection of 25 deg is shown in Fig. 34. Peak heating on the cavity behind the flaps

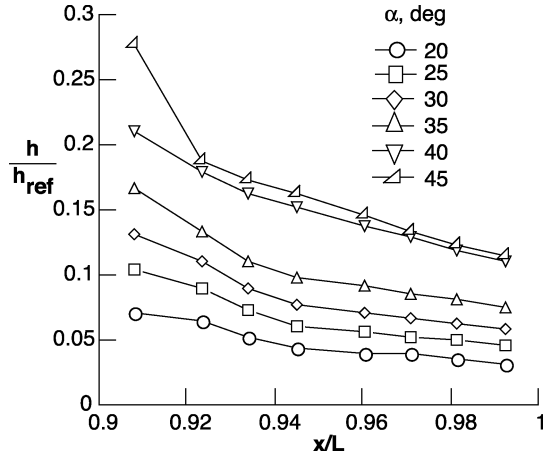


**Fig. 34 Effect of angle of attack on X-38 Rev 8.3 centerline cavity floor heating distribution: $M_\infty$ = 6 air, $Re_{\infty,L} = 8 \times 10^6$, and $\delta_{BF}$ = 25 deg.**

approached 30% of reference stagnation values at 45-deg angle of attack (Fig. 34). Incidence angles greater than 40 deg were being considered for hypersonic entry to moderate heating caused by vehicle weight growth. It is reasonable to assume that the flap cavity interface might see significant heating if roll control authority requires flap deflections between 10 and 15 deg at these higher entry angles of attack. The original design environment for this area had been compiled completely from LaRC experimental wind-tunnel data. The measured heating distributions were invaluable in developing a thermal design model and flight scaling factors applicable to this localized region.

### Boundary-Layer Transition

The proposed TPS of the X-38 windward surface consists of shuttle-like ceramic tiles, and, similar to orbiter flight experience, boundary-layer transition is expected to be roughness dominated. Surface roughness can arise from inherent TPS tile mismatch because of manufacturing tolerances or can result from protruding gap filler material. Experimental efforts[18,54] were made to determine whether X-38 boundary-layer transition could be forced from discrete roughness. The analysis of data from Ref. 18 has been used to quantify the effects of isolated roughness along the centerline of the windward surface and to develop a transition correlation for the X-38 vehicle. Information from such a correlation has been used to provide manufacturing guidelines and constraints for the step and gap tolerances of the TPS tiles and carrier panels. With such step tolerances defined, an estimate of when boundary-layer transition should occur in flight can be made.

The experimentally determined transition correlation was developed using the same methodology reported in Ref. 19. Phosphor heating images were used to identify the transition footprint located downstream of systematically placed roughness elements. The roughness elements used in this study were fabricated from an adhesively backed polyimide film cut to simulate the planform shape of a raised TPS tile. Variations of the roughness height $k$ were made by stacking multiple layers of the tape. (Heights of 0.0025, 0.005, and 0.0075 in. were typically used.) The size, height, and location of the discrete tripping devices were methodically varied as was freestream unit Reynolds number in order to produce transitional and fully turbulent flow (see Ref. 18 for complete details). Laminar boundary-layer edge conditions at the trip location were computed using a boundary-layer code[60] (LATCH) for a range of Reynolds numbers. To correlate the data, the experimental transition results were compared using the transition parameter of momentum thickness Reynolds number divided by edge Mach number ($Re_\theta/M_e$) and the disturbance parameter of roughness height divided by boundary-layer thickness $k/\delta$. Figure 35 provides the results of this correlation for all of the discrete trip results along the X-38 centerline for Mach 6 for an angle of attack of 40 deg. Curve fits representing Mach 6 transition onset and fully turbulent flow have been experimentally

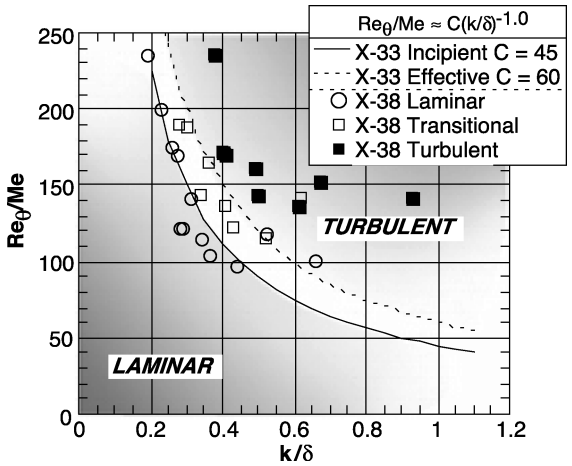


**Fig. 35 Experimental transition correlation of X-38 Rev 3.1 windward centerline discrete roughness data and comparison with X-33 results[61]: $M_\infty$ = 6 air, and $\alpha$ = 40 deg.**

determined for X-33[61] and are superimposed on the X-38 data set for comparative purposes. The correlated X-38 data are consistent with that determined for X-33. It is well known that the determination of transition onset from discrete roughness can be influenced by tunnel noise[62] and that the incipient transition curve defined in Fig. 35 can be conservative. The current X-38 TPS manufacturing guidelines specify step tolerances no larger than 0.08 in. (full scale) near the nose cap on the windward surface.

### Extrapolation to Flight

A feature of the phosphor thermography analysis package[26] (IHEAT) is the ability to extrapolate ground-based heating measurements to flight radiation equilibrium wall temperatures. The successful application of this technique to predict Mach 6 flight surface temperatures for both laminar and turbulent conditions was demonstrated in the X-34[26,27] and X-33[29] programs and later to shuttle flight measurements at Mach 5 and 11.[63] Based on the successful Mach 6 extrapolation of X-33 and X-34 wind-tunnel data (at the time this paper was originally submitted) and the good agreement between the X-38 measurement and prediction presented in this report, phosphor data were extrapolated to flight surface temperatures at Mach 6 and 10. Comparison of extrapolated data to turbulent Mach 6 and laminar equilibrium Mach 10 flight prediction are shown in Figs. 36 and 37. The Mach 6 tunnel data were obtained on Rev 8.3 at $\alpha = 40$ deg, flap deflection of 20 deg, and $Re_{\infty,L} = 4 \times 10^6$, where turbulence was forced with discrete roughness. Mach 6 flight conditions at $\alpha = 40$ deg correspond to an altitude of 127,000 ft; velocity of 6226 ft/s; and a length Reynolds number of $5 \times 10^6$. The Mach 10 tunnel data were obtained on Rev 3.1 at $\alpha = 40$ deg, flap deflection of 25 deg, and $Re_{\infty,L} = 1 \times 10^6$. Mach 10 flight conditions at $\alpha = 40$ deg correspond to an altitude of 157,000 ft; velocity of 11,361 ft/s; and a length Reynolds number of $2.3 \times 10^6$. No significant real-gas aeroheating effects were anticipated at the Mach 6 and 10 X-38 flight conditions.

The extrapolated phosphor images were mapped to the three-dimensional vehicle surface geometry with the IHEAT code Map3D tool. This mapping technique permits a more accurate spatial representation of the global data, particularly when extraction and comparison with numerical prediction are desired. The turbulent extrapolated surface temperatures at Mach 6 agreed quite well (within 5%) relative to predicted flight temperatures (Fig. 36a) with the exception of the body-flap region. Consistent with the poor agreement found in the wind-tunnel comparisons (Fig. 26b), the Baldwin–Lomax algebraic turbulence model used for the flight computation underpredicts the extrapolated (experimental) temperatures on the deflected body flap, as shown in Fig. 36b. Comparison of extrapolated temperature with turbulent prediction along an axial station well upstream of the expansion surface and deflected flaps (Fig. 36c) were in much better agreement.

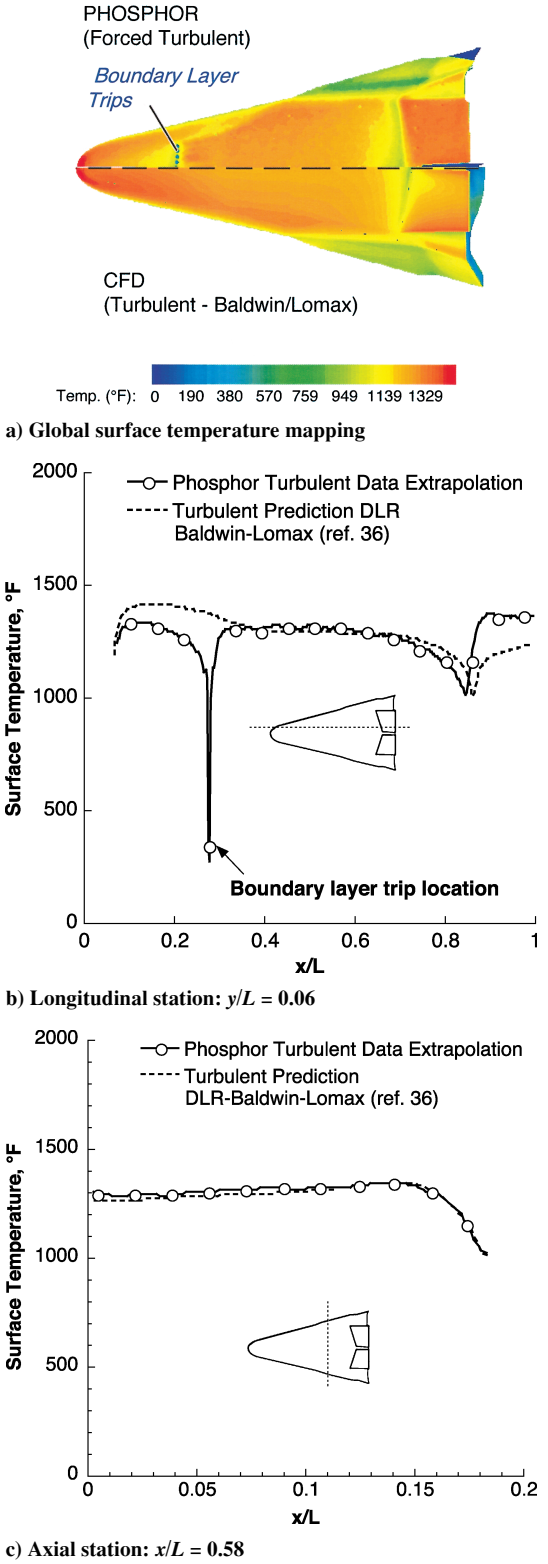


**Fig. 36 Comparison of extrapolated turbulent experimental data with turbulent flight prediction[36]: $M_\infty$ = 6, $\alpha$ = 40 deg, $\delta_{BF}$ = 20 deg, and $Re_{\infty,L} = 5 \times 10^6$.**

The excellent comparison of laminar extrapolated temperature at Mach 10 to flight prediction (Fig. 37) illustrates the versatility of the extrapolation theory and has extended the demonstrated range of applicability to Mach 10. Similar to the Mach 6 data, the surface temperatures compared well over the entire image with the exception of the body flap. This observation was not surprising, as the extent of laminar separation was not captured computationally at wind-tunnel conditions (see Fig. 13). Upstream of the flap

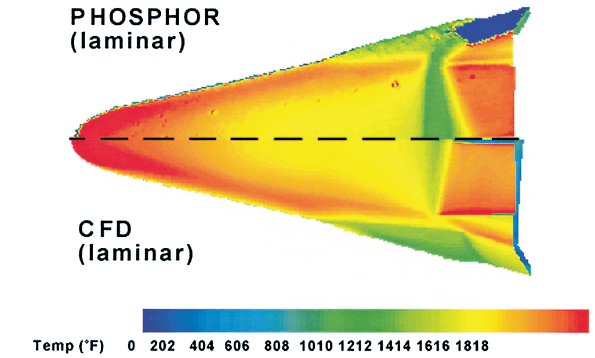


a) Global surface temperature mapping

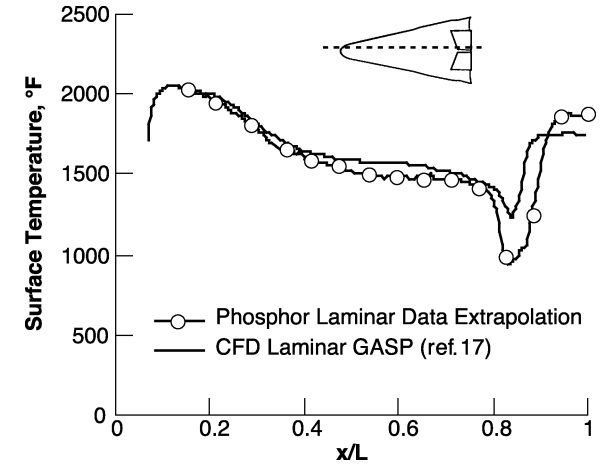


b) Longitudinal station: $y/L = 0.06$

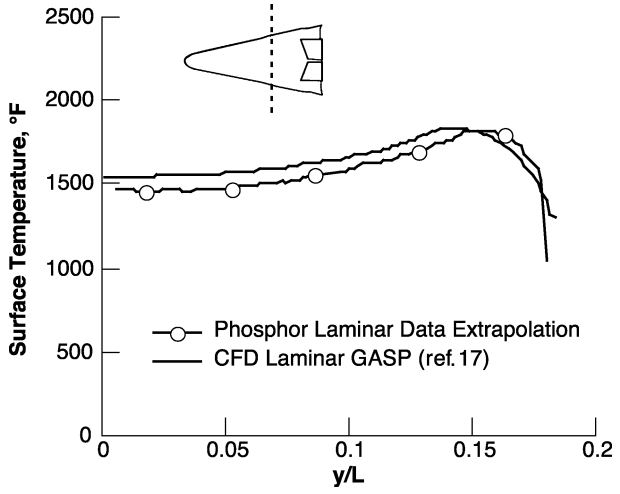


c) Axial station: $x/L = 0.58$

**Fig. 37 Comparison of extrapolated laminar experimental data with laminar flight prediction[36]: $M_\infty = 10$, $\alpha = 40$ deg, $\delta_{BF} = 25$ deg, and $Re_{\infty,L} = 5 \times 10^6$.**

interaction, the extrapolated wind-tunnel data at Mach 6 and 10 generally compared to within 50°F (or better) of flight prediction levels. The extrapolation methodology has the potential to provide detailed and timely design information early in a design cycle, when a large number of vehicle parametrics are being considered. This type of experimentally derived global information provided to the designer early in the TPS evaluation process would be invaluable for material selection and sizing requirements.

## Conclusions

This report provides an overview of the hypersonic aerothermodynamic wind-tunnel program conducted at the NASA Langley Research Center (LaRC) to date by the Aerothermodynamics Branch in support of the X-38 vehicle design. The X-38 program was able to take advantage of recent developments in a two-color global phosphor thermography technique, providing an opportunity to conduct heating screening/trade studies concurrent with aerodynamic tests. The LaRC ground tests contributed significantly to the development and validation of the flight data book for longitudinal and lateral aerodynamic characteristics as well as control-surface effectiveness. Comparison of aerodynamic measurements between Mach 6 air and $CF_4$, provided an indication of the significance of real-gas effects for X-38. Global and discrete surface heat-transfer measurements were primarily used in the continued development and validation of computational tools used to predict the X-38 aeroheating environment. Under the present NASA/European partnership, the aerodynamic and heating measurements provided by LaRC were utilized to augment and compliment test results obtained in European facilities. The synergism between the experimental and computational work performed within the X-38 program has led to an improved understanding of complex flows associated with this vehicle configuration.

The hypersonic aerodynamic wind-tunnel tests indicated that the X-38 has more than sufficient control authority for pitch control. Pitching-moment increments from the LaRC Mach 6 and 10 tests compared favorably with the data-book values derived from European aerodynamic tests. Heavy-gas simulation tests have indicated that real-gas effects on X-38 aerodynamics at trim conditions are expected to primarily influence flap effectiveness. Relative to laminar perfect-gas results, the heavy-gas simulation tests revealed an increase in body-flap effectiveness across the angle-of-attack range.

Global heating measurements for attached laminar flows were in good agreement with predictions from CFD codes used to define the flight aeroheating environment. Experimental heating measurements in the vicinity of control surfaces (body flaps and rudder) were made to provide initial design information from which thermal margin assessments were made. Predicted deflected flap heating distributions were compared to measured heating data from the LaRC tests in an effort to develop a higher degree of confidence in predictive techniques utilized for separating reattaching flows. Transitional flow reattachment represented a challenge from a numerical modeling perspective. In areas where predictive tools could not provide accurate information, such as the cavity behind the deflected flaps, the design environment has been compiled completely from LaRC experimental wind-tunnel data. The heating distributions on the cavity floor were invaluable in developing a thermal design model and flight scaling factors applicable to this localized region. Future computational work and experimental tests are anticipated to refine this model and further reduce uncertainties. A more comprehensive experimental and computational effort has been initiated to more accurately predict the flight-heating environment associated with the windward surface of the deflected body flaps.

The global aeroheating results obtained at Mach 6 have been used to quantify the effects of isolated roughness along the centerline of the windward surface and to develop a boundary-layer transition correlation for the X-38 vehicle. Information from the correlation was used to provide manufacturing guidelines for step and gap tolerances of the thermal-protection-system (TPS) tiles and carrier panels. With such step tolerances defined, estimates of when boundary-layer transition would occur in flight can be made.

Extrapolation of wind-tunnel heating measurements to flight radiation equilibrium wall temperatures were made at Mach 6 and 10. The extrapolated wind-tunnel data generally compare to within 50°F (or better) of flight prediction. This type of information would be invaluable and could potentially result in significant savings of computational time required for flight predictions if provided to the designer early in the TPS evaluation process.

## Acknowledgments

Without the assistance of the following individuals, this work would not have been possible: Mark Cagle, Joe Powers, Mike Powers, Mark Griffith, Ed Covington, and Tom Burns for model design, fabrication, instrumentation, and surface inspection support;

John Ellis, Rhonda Manis, Grace Gleason, Melanie Lawhorne, Harry Stotler, Steve Jones, and Jeff Werner for wind-tunnel support; Sheila Wright and Bert Senter for data-acquisition assistance; Tuan Trong, Leo Perez, Chuck Campbell, and Steve Labbe for analysis support; The German Aerospace Center and the partners of the German national program on reentry technologies (TETRA) for (computational-fluid-dynamics) support; Dassault Aviation for the two-layer laminar and turbulent wind-tunnel heating predictions; and Richard Wheless for documentation assistance. The authors gratefully acknowledge their contributions and behind-the-scenes work.

## References

[1]Brown, D., "Manning the Lifeboats on the International Space Station," *Launchspace*, Vol. 3, No. 2, 1998, pp. 20–22.

[2]Asker, J. R., "For Myriad of Woes, NASA Calls X-38 to the Rescue," *Aviation Week and Space Technology*, Vol. 145, No. 20, 1996, pp. 70–71.

[3]de Selding, P. B., "ESA, United States Advance Toward Common Crew Craft," *Space News*, 18–24 Nov. 1996, p. 3.

[4]de Selding, P. B., "Germany, NASA Pen Deal for Crew Lifeboat Work," *Space News*, 24–30 Nov. 1997.

[5]Smith, B. A., "Weather May Hamper X-38 Drop Tests," *Aviation Week and Space Technology*, Vol. 147, No. 24, 1997, p. 33.

[6]Kandebo, S. W., "Vista F-16 Tests Preview X-38 Flight Controls," *Aviation Week and Space Technology*, Vol. 149, No. 16, 1998, p. 41.

[7]Covault, C., "Second X-38 Set for Flight," *Aviation Week and Space Technology*, Vol. 149, No. 9, 1998, p. 58.

[8]Reed, R. D., "Wingless Flight The Lifting Body Story," NASA SP-4220, 1997.

[9]Barret, C., "Lifting Body Stability and Control," NASA TM–1999-209255, March 1999.

[10]"SV-5D Prime Final Flight Test Summary," Martin Marietta Engineering, Rept. ER 14465, Baltimore, MD, Sept. 1967.

[11]"Prime Follow-on Program: Addition Aerodynamic and Aerothermodynamic Data Analysis," Martin Marietta Engineering, Rept. ER 14686, Denver, CO, Jan. 1968.

[12]Hallion, R. P., *The Hypersonic Revolution: Eight Case Studies in the History of Hypersonic Technology*, Vol. 2 Aeronautical Systems Div., Wright–Patterson AFB, OH, 1987, pp. 893–923.

[13]Dornhiem, M. A., "X-38 Transitions from Lifting Body to Parafoil," *Aviation Week and Space Technology*, Vol. 148, No. 12, 1998, p. 92.

[14]Labbe, S. G., Perez, L. F., Fitzgerald, S. M., Longo, J. M. A., and Rapuc, M., "X-38 NASA/DLR/ESA-Dassault Aviation Integrated Aerodynamic and Aerothermodynamics Activities," *Proceedings of the Atmospheric Reentry Vehicle and Systems Symposium*, French Association for Aeronautics and Astronautics, Arachon, France, 1999.

[15]Tribot, J. P., Tran, P., Pallegoix, J. F., Orlowski, M., Bruck, S., Andres, O. P., and Fitzgerald, S. M., "X-38 Aerothermodynamics," *Proceedings of the Atmospheric Reentry Vehicle and Systems Symposium*, French Association for Aeronautics and Astronautics, Arachon, France, 1999.

[16]Campbell, C. H., Caram, J. M., Berry, S. A., Horvath, T. J., Merski, N. R., Loomis, M. P., and Venkatapathy, E., "An Overview of X-38 Hypersonic Aerothermodynamic Wind Tunnel Data and Comparison with Numerical Results," AIAA Paper 97-2475, June 1997.

[17]Loomis, M. P., Venkatapathy, E., Papadopoulos, P., Davies, C. B., Berry, S. A., Horvath, T. J., and Campbell, C. H., "Aeroheating and Aerodynamic CFD Validation and Prediction for the Computational/Experimental Aeroheating Predictions for the X-38 Program," AIAA Paper 97-2478, June 1997.

[18]Berry, S. A., Horvath, T. J., Roback, V. E., and Williams, G. B., "Results of Aerothermodynamic and Boundary-Layer Transition Testing of 0.0362-Scale X-38 (Rev. 3.1) Vehicle in NASA Langley 20-Inch Mach 6 Tunnel," NASA TM-112857, Sept. 1997.

[19]Berry, S. A., and Hamilton, H. H., "Discrete Roughness Effects on Shuttle Orbiter at Mach 6," AIAA Paper 2002-2744, June 2002.

[20]Campbell, C. H., Caram, J. M., Berry, S. A., Horvath, T. J., and DiFulvio, M., "Overview of X-38 Hypersonic Wind Tunnel Data and Comparison with Numerical Results," AIAA Paper 97-0567, Jan. 1997.

[21]Miller, C. G., "Development of X-33/X-34 Aerothermodynamic Data Bases: Lessons Learned and Future Enhancements," Applied Vehicle Technology Symposium Aerodynamic Design and Optimization of Flight Vehicles in a Concurrent Multi-Disciplinary Environment, NATO Research and Tech. Organization, Paper 32, Oct. 1999.

[22]Miller, C. G., "Langley Hypersonic Aerodynamic/Aerothermodynamic Testing Capabilities—Present and Future," AIAA Paper 90-1376, June 1990.

[23]Buck, G. M., "Rapid Model Fabrication and Testing for Aerospace Vehicles," AIAA Paper 2000-0826, Jan. 2000.

[24]Buck, G. M., and Vasquez, P., "An Investment Ceramic Slip-Casting Technique for Net-Form, Precision, Detailed Casting of Ceramic Models," U.S. Patent 5,266,252, 30 Nov. 1993.

[25]Buck, G. M., "Automated Thermal Mapping Techniques Using Chromatic Image Analysis," NASA TM 101554, April 1989.

[26]Merski, N. R., "Reduction and Analysis of Phosphor Thermography Data with the IHEAT Software Package," AIAA Paper 98-0712, Jan. 1998.

[27]Merski, N. R., "Global Aeroheating Wind-Tunnel Measurements Using Improved Two-Color Phosphor Thermography Method," *Journal of Spacecraft and Rockets*, Vol. 36, No. 2, 1998, pp. 160–170.

[28]Berry, S. A., Horvath, T. J., DiFulvio, M., Glass, C., and Merski, N. R., "X-34 Experimental Aeroheating at Mach 6 and 10," *Journal of Spacecraft and Rockets*, Vol. 36, No. 2, 1998, pp. 171–178.

[29]Horvath, T. J., Berry, S. A., Hollis, B. R., Liechty, D. S., and Merski, N. R., "X-33 Experimental Aeroheating at Mach 6 Using Phosphor Thermography," *Journal of Spacecraft and Rockets*, Vol. 38, No. 5, 2001, pp. 634–645.

[30]Miller, C. G., III, "Comparison of Thin-Film Resistance Heat-Transfer Gages with Thin-Skin Transient Calorimeter Gages in Conventional Hypersonic Wind Tunnels," NASA TM 83197, Dec. 1981.

[31]Hollis, B. R., "User's Manual for the One-Dimensional Hypersonic Experimental Aero-Thermodynamic (1DHEAT) Data Reduction Code," NASA CR 4691, Aug. 1995.

[32]Cook, W. J., "Unsteady Heat Transfer Measurements to a Semi-Infinite Solid with Arbitrary Surface Temperature History and Variable Thermal Properties," Iowa State Univ, Technical Rept. ISU-ERI-AMES-67500, Feb. 1970.

[33]Kendall, D. N., Dixon, W. P., and Schulte, E. H., " Semiconductor Surface Thermocouples for Determining Heat-Transfer Rates," *IEEE Transactions on Aerospace and Electronic Systems*, Vol. AES-3, No. 4, 1967, pp. 596–603.

[34]Hollis, B. R., " Experimental and Computational Aerothermodynamics of a Mars Entry Vehicle," Ph.D. Dissertation, North Carolina State Univ., (Grants NAG1-1663, NAGW-1331, Raleigh, NC, Dec. 1996.

[35]Kline, S., and McClintock, F., "Describing Uncertainties in Simple Experiments," *Mechanical Engineering*, Vol. 75, No. 1, 1953, pp. 3–8.

[36]Fitzgerald, S. M., "X-38/CRV Aerothermal Databook," NASA Rept. 29047, June 2000.

[37]Tribot, J. P., "X-38 Step 2 Aerothermodynamic Data Base," Dassault Aviation, Rept. DGT 77469, Jan. 1999.

[38]Bruck, S., Eggers, T., Longo, J. M., and Orlowski, M., "Investigation of Hypersonic Flows past the NASA X-24 Lifting Body Vehicle," Deutsches Zentrum fur Luft-und Raumfahrt, DLR IB 129-97/7, July 1997.

[39]Orlowski, M., Ludeke, V., Longo, J., Giese, P., and Bruck, S., "Contribution of DLR to the Aerodynamic Data Base of the X-38 Vehicle," Deutsches Zentrum fur Luft-und Raumfahrt, DLR IB 129-98/8, Aug. 1998.

[40]Bruck, S., Giese, P., Hannemann, V., Ludeke, H., and Orlowski, M., "Contribution of DLR to the Aerodynamic and Aerothermodynamic Data Base of the X-38 Vehicle," Deutsches Zentrum fur Luft-und Raumfahrt, DLR IB 129-99/12, Dec. 1999.

[41]Fay, J. A., and Riddell, F. R., "Theory of Stagnation Point Heat Transfer in Dissociated Air," *Journal of Aeronautical Sciences*, Vol. 25, No. 2, 1958, pp. 73–85.

[42]Michel, F. C., "Aerodynamic Data Book- SV-5D Aerodynamic Characteristics. 680A Program," Martin Marietta, CR-113 E, 5th rev, Baltimore, MD, Oct. 1965.

[43]Murphy, K., Nowak, R., Thompson, R. A., and Hollis, B. R., "X-33 Hypersonic Aerodynamic Characteristics," *Journal of Spacecraft and Rockets*, Vol. 38, No. 5, 2001, pp. 670–683.

[44]Hollis, B. R., Thompson, R. A., Murphy, K. J., Nowak, R. J., Riley, C. J., Wood, W. A., Alter, S. J., and Prabhu, R. K., "X-33 Aerodynamic Computations and Comparisons with Wind Tunnel Data," *Journal of Spacecraft and Rockets*, Vol. 38, No. 5, 2001, pp. 684–691.

[45]Thompson, R. A., "Review of X-33 Hypersonic Aerodynamic and Aerothermodynamic Development," *Proceedings of the 22nd International Congress of the Aeronautical Sciences*, ICA-0323, International Council of Aeronautical Sciences, Harrogate, England, U.K., 2000, pp. 323.1–323.19.

[46]Brauckmann, G. J., Paulson, J. W., and Weilmuenster, J. K., "Experimental and Computational Analysis of Shuttle Orbiter Hypersonic Trim Anomaly," *Journal of Spacecraft and Rockets*, Vol. 32, No. 5, 1995, pp. 758–764.

[47]Perez, L. F., "X-38 Aerodynamic Design Data Book," NASA Rept. 28854, Rev. G, Feb. 2000.

[48]Heppenheimer, T. A., "The Space Shuttle Decision. NASAs Search for a Reusable Space Vehicle," NASA SP-4221, 1999.

[49]Screen, E. N., and Nickel, H. S., "Hypersonic Heat Transfer Test Results From a 9.688% Model SV-5D Vehicle For Program 680A In the Martin Hypersonic Tunnel-Second Series," Martin Co., Baltimore Div., ER-13686, Baltimore, MD, Feb. 1965.

[50]Wong, H., and Kremer, F., "Numerical Assessment on the Heating of the Rudder/Fin Gap in the X-38 Space Vehicle," *Proceedings of the Atmospheric Reentry Vehicle and Systems Symposium*, French Association for Aeronautics and Astronautics, Arachon, France, 1999.

[51]Muhlrazer, A., Frohlich, A., and Wildenrotter, K., "Design, Material and Manufacturing Aspects of the X-38 Body Flaps," *Proceedings of the Atmospheric Reentry Vehicle and Systems Symposium*, French Association for Aeronautics and Astronautics, Arachon, France, 1999.

[52]Trabandt, U., Schmid, T., Reinkober, H., and Ritter, H., "Light-Weight CMC TPS for Future RLV Applied on X-38 Nose Skirt," *Proceedings of the Atmospheric Reentry Vehicle and Systems Symposium*, French Association for Aeronautics and Astronautics, Arachon, France, 1999.

[53]Bruek, S., Radespiel, R., and Longo, J., "Comparison of Nonequilibrium Flows past a Simplified Space-Shuttle Configuration," AIAA Paper 97-0275, Jan. 1997.

[54]Berry, S. A., Horvath, T. J., Weilmuenster, K. J., Alter, S. J., and Merski, N. R., "X-38 Experimental Aeroheating at Mach 10," *Journal of Spacecraft and Rockets*, Vol. 41, No. 2, 2004, pp. 293–301.

[55]Simeonides, G., "Hypersonic Shock Wave Boundary Layer Interactions over Simplified Deflected Control Surface Configurations," Special Short Course on Shock-Wave/Boundary-Layer Interactions in Supersonic and Hypersonic Flows, AGARD R-792, Aug. 1993.

[56]Ludeke, H., and Krogmann, P., "Numerical and Experimental Investigations of Laminar/Turbulent Boundary Layer Transition," *Proceedings of the 6th European Congress on Computational Methods in Applied Sciences and Engineering*, European Congress on Computational Methods, Barcelona, 2000.

[57]Rhudy, R., and Merz, G., "Heat Transfer and Pressure Distribution on a Scale Model SV-5D at Mach 10," U. S. Air Force Arnold Engineering Development Center, AEDC-TR-194, Tullahoma, TN, Sept. 1965.

[58]Weber, C., Behr, R., and Weiland, C., "Investigation of Hypersonic Turbulent Flow Over the X-38 Crew Return Vehicle," AIAA Paper 2000-2601, June 2000.

[59]Delattre, N., Coron, F., Jacquelard, C., Hollanders, H., Lemaire, D., and Moules, G., "Numerical Prediction of Hypersonic Reacting Flows with the Finite Volume Solver FLU3NEQV," AIAA Paper 97-0343, Sept. 1997.

[60]Hamilton, H., Green, F., and DeJarnette, F., "Approximate Method for Calculating Heating Rates on Three-Dimensional Vehicles," *Journal of Spacecraft and Rockets*, Vol. 31, No. 3, 1994, pp. 345–354.

[61]Berry, S. A., Horvath, T. J., Hollis, B. R., Thompson, R. A., and Hamilton, H. H., "X-33 Hypersonic Boundary Layer Transition," *Journal of Spacecraft and Rockets*, Vol. 38, No. 5, 2001, pp. 646–657.

[62]Schneider, S. P., "Effects of High-Speed Tunnel Noise on Laminar-Turbulent Transition," *Journal of Spacecraft and Rockets*, Vol 38, No. 3, 2001, pp. 323–333.

[63]Berry, S. A., Merski, N. R., and Blanchard, R. C., "Wind Tunnel Measurements of Shuttle Orbiter Global Heating with Comparison to Flight," AIAA Paper 2002-4701, Aug. 2002.

M. Torres
*Associate Editor*

**Color reproductions courtesy of NASA Langley Research Center.**